Mechanism and Machine Theory 228 (2026) 106564

Contents lists available at ScienceDirect

Mechanism and Machine Theory

journal homepage: www.elsevier.com/locate/mechmt

Research paper

Indirect measurement of railway pantograph contact force using model-based and data-driven approaches in laboratory tests

J. Gil [a,*], M. Tur [a], S. Gregori [a], F. J. Fuenmayor [a]

[a] Mechanical and Biomechanical Engineering University Research Institute (I2MB), Universitat Politècnica de València, Camino de Vera s/n, Valencia, 46022, Spain

ARTICLE INFO

Keywords:
Inverse dynamic problem
Pantograph-catenary
LSTM
Augmented Kalman filter
Neuronal network
Hyper-parameter optimisation

ABSTRACT

The contact force between the pantograph and the overhead contact line is a key indicator of railway current collection performance. Conventional measurement techniques rely on instrumented pantographs with structural modifications, increasing system complexity and limiting practical implementation. This work proposes and experimentally validates a low-intrusive methodology to estimate the pantograph contact force using acceleration, displacement, and pressure measurements while avoiding force measurements.

The estimation problem is separated into two frequency ranges. The very low-frequency component is reconstructed from the pressure signal of the pantograph uplift mechanism, while the remaining frequency content is obtained by solving an inverse dynamic problem based on displacement and acceleration measurements. Four estimation models are investigated: two model-based approaches (Kalman Filter and Moving Horizon Estimation) and two data-driven models (feedforward Neural Network and Long Short-Term Memory network). Model parameters and hyperparameters are optimised to ensure a fair comparison and fully exploit the models' potential.

The methodology is experimentally validated on a laboratory test bench with a real pantograph. Results show reconstruction of the contact force within the 0–20 Hz range defined by EN 50317.

1. Introduction

1.1. Background

The pantograph is a mechanism responsible for supplying energy to electric trains through sliding contact with the overhead contact line (OCL), also known as catenary. The mechanical performance of this system is primarily assessed through the contact force (CF) at the pantograph–catenary interface, which varies over time. For this reason, simulation tools have been developed [1], and there is also significant interest in contact force measurement for homologation and monitoring purposes [2].

Direct measurement of the contact force is not feasible due to the sliding nature of the contact; therefore, indirect measurement techniques must be employed. Currently, this is achieved using instrumented pantographs that measure forces and apply wind and inertia corrections procedures to estimate the contact force. The main drawback of this technique is that the pantograph must be structurally modified to enable force measurements, preventing monitoring tasks by mass produced pantographs. Consequently, there is growing interest in developing alternative, low-intrusive methods that do not alter the pantograph structure.

* Corresponding author.
E-mail address: jaigiro@upv.es (J. Gil).

https://doi.org/10.1016/j.mechmachtheory.2026.106564
Received 23 March 2026; Received in revised form 24 July 2026; Accepted 25 July 2026
Available online 4 August 2026
0094-114X/© 2026 The Author(s). Published by Elsevier Ltd. This is an open access article under the CC BY-NC license (http://creativecommons.org/licenses/by-nc/4.0/).

1.2. Problem of interest

This paper focuses on the problem of measuring the contact force acting on an operating pantograph while avoiding any modification of its structural components. Consequently, only acceleration and displacement sensors are considered for the indirect estimation of the contact force. This requires solving an inverse dynamic problem, either through classical model-based approaches or by means of data-driven artificial intelligence models. Since the mean value of the contact force and also the very low frequency content cannot be inferred from acceleration or displacement measurements alone, the pressure signal of the pantograph uplift mechanism is used for this purpose.

This work aims to be experimental, where the measurement method is applied to a real pantograph in a laboratory environment. This setup allows the force to be not only estimated, but also directly measured to assess the performance of the proposed estimation method.

According to the current standard EN 50317 [2], contact force measurement shall be performed in the 0–20 Hz range. Thus, this work also focuses on this frequency range.

1.3. State of the art

Model-bases force estimation methods

The use of Kalman-filter-based techniques [3] for indirect force estimation has received considerable attention in structural dynamics, as these methods enable the recovery of unknown excitation forces from noisy measurements of displacement, velocity, or acceleration. One of the most widely adopted approaches is the state-augmentation (Augmented Kalman filter) strategy [4], in which the unknown input is modelled as an additional state driven by a stochastic process. The formulation is broadly applicable, but its performance strongly depends on the assumed dynamics of the augmented force states. Incorrect modelling may lead to over-smoothing, artificial dynamics, or loss of identifiability. An alternative to the augmented-state strategy is the family of unbiased minimum-variance (UMV) estimators [5]. Darouach et al. [6] introduced a UMV Kalman filter capable of estimating states and unknown inputs without augmenting the state vector. While efficient, the method requires the system matrices to satisfy a set of conditions. A comprehensive list of Kalman-filter-based methods for unknown-input systems is provided by Pan et al. [7]. Their work surveys a broad range of formulations, including: the classical UMV estimators [8]; two-stage projection-based filters [9], which first remove the influence of unknown inputs from the measurement equation and subsequently apply a standard Kalman filter; the Extended Kalman Filter (EKF) or the Unscented Kalman Filter (UKF) for non-linear systems. Liu and Shepard [10] presented an inverse method capable of estimating unknown inputs in systems with strong non-linearities, including state-dependent stiffness and non-linear damping. Their approach combines iterative linearisation with Kalman filtering concepts, effectively enabling force estimation in scenarios where linear models are insufficient. However, these non-linear methods exhibit sensitivity to linearisation errors, rely on accurate modelling, and may require iterative tuning of noise covariances to achieve stable performance.

Data-driven force estimation methods

More recent data-driven artificial intelligence (AI) models have been adopted to address inverse dynamic or force estimation problems, particularly in systems where classical model-based approaches such as Kalman filtering face limitations due to modelling difficulties. Furthermore, the implementation of AI implementation in general is faster because the need for explicit physical modelling is avoided. Some works typically rely on feed-forward artificial neural networks (ANNs) trained to approximate the relation between temporal signals such as measured system responses and unknown excitations. For instance, a estimator for the external torque of a manipulator (robot) using an ANN fed with the position, velocity and torque of the joints was implemented successfully in [11]. The use of an ANN incorporating the physical model is proposed by [12] implementing a Physics-Informed ANN (PINN) for recovering the input force acting on a non-linear single-degree-of-freedom model. In their formulation, the governing differential equation is embedded directly into the loss function, ensuring that the trained model fulfils physical consistency. This approach improves robustness especially when only partial measurements are available.

According to the nature of the problem of interest the architecture of Recurrent Neural Networks (RNNs) is particularly suitable. Among them, one of the most widely used variants is the Long Short-Term Memory (LSTM) network [13]. In [14], LSTMs are implemented to recover external torques in articulated robots exhibiting non-linearities such as joint hysteresis and friction, and their performance is compared with alternative architectures such as Multilayer Perceptrons (MLPs). The LSTM net is combined with a rigid-body physical model to compute the variables that can be determined directly which feed the LSTM. The whole hybrid model therefore uses joint position, velocity, and acceleration as inputs. In [15], a velocity-aware spatio-temporal attention LSTM architecture for predicting joint torques of robotic manipulators based on joint position, velocity, and acceleration, was proposed. The model integrates two attention mechanisms: a spatial attention module, which weights the input features, and a temporal attention module, which weights the previous hidden states of the LSTM for computing the output. Both attention mechanisms explicitly incorporate joint velocity information, implementing the velocity-aware design.

Beyond classical manipulator systems, in [16] a Distance-Assisted Graph Neural Network (DA-GNN) was introduced for reconstructing and localizing impact forces in structural components instrumented with distributed sensors. In this formulation, sensors are treated as nodes in a graph, and spatial relationships are encoded through distance-aware adjacency matrices. This enables the GNN to learn how impact forces propagate across the structure, achieving high accuracy in both estimation and localization.

Pantograph-catenary

The procedure for measuring the contact force in the pantograph-catenary system is regulated with the European Standard EN-50317 [2]. According with this Standard, the CF has to be measured with force transducers placed the closest to the contact surface.

The difference between the contact force and the measured force is supposed to be produced by the inertial forces of the mass between the transducer and the contact surface and aerodynamic forces, thus, a correction is done with additional measurements of acceleration and aerodynamic forces. This procedure is followed by the industry and there are works with its implementation, as in [17], where Fibre Bragg Gratings sensors are compared to electrical sensors, revealing certain variability in the results with both sensor configurations, which shows the challenging nature of the indirect contact force measurement. Although the Standard EN-50317 [2] does not contemplate alternative methods to avoid the use of force transducers, it sets a validation procedure, so new alternatives can be verified.

Currently, there is a predominance of traditional systems such as the well-established monitoring system used in China's high-speed railways [18] to measure several magnitudes as the CF, with a 5 N precision, and other phenomena as arching. However, there are also some works trying to avoid pantograph modifications to measure the CF. In [19], an inversion method is presented for estimating the contact force with strain measurement in the pantograph contact strips. Others authors [20,21], consider the acceleration measures on the pantograph for monitoring purposes avoiding an estimation of the contact force. In [22], an Augmented Kalman Filter (AKF) is used to predict the contact force inputting the acceleration and displacement signals. In this case, a pantograph linear model with a simplified catenary is included. In [23], also the KF approach is used to predict the pantograph CF through displacement measurements obtained by camera. In that work the Least Square Recursive approach is combined with a Kalman filter, following the strategy propose in [24], for improving accuracy, and a linear lumped-mass pantograph model is considered.

The use of AI models is also employed in the pantograph-catenary system. For example, the use of ANNs [25], LSTM networks [26] or physics-based machine learning models [27] as surrogate models was proposed to reduce the computational cost of pantograph-catenary dynamic simulation. Also in [28], LSTM networks are used to replace the time integration scheme in the pantograph-catenary dynamic interaction problem. In [29], a Search Algorithm–Radial Basis Function (SCSA-RBF) network is developed as a surrogate model of the panhead acceleration. A close application to the problem of interest can be found in [30], where ANNs are used for the prediction of CF statistics by the measurement of acceleration signals. The method was tested in a simulated and a laboratory environment with a real pantograph, showing the first better accuracy. The only data-driven model found in the literature for solving the inverse dynamic problem of the pantograph was proposed in [31]. A hybrid GRU model combined with a one-dimensional convolutional neural network (CNN-GRU) is used to predict the CF from pantograph displacement and acceleration data.

1.4. Contributions

This work proposes a low-intrusive procedure for estimating the contact force acting on a pantograph using not only measurements of acceleration and displacement of the contact strip center, but also the pressure of the uplift mechanism. While the very low-frequency components of the contact force (below 0.5 Hz) are captured with the pressure signal, the acceleration and displacement measurements are used to estimate the force over the remaining frequency range.

This study investigates and compares four different estimation models: two model-based approaches, Kalman filter (KF) and Moving Horizon Estimation (MHE); and two data-driven artificial intelligence models, a feedforward Neural Network (NN) and a Long Short-Term Memory network (LSTM).

The key contributions of this work are summarized as follows:

- This work advances the state of the art in pantograph contact force monitoring by introducing and experimentally validating a low-intrusive estimation framework using experimental data obtained from a laboratory test bench with a real pantograph (DSA-380).
- Whereas existing methods mainly rely on acceleration and displacement measurements, this work also uses the pressure signal to reconstruct the low-frequency component of the contact force.
- This work provides a systematic comparison between model-based and artificial intelligence methods under identical conditions.
- For the KF approach, several implementation strategies are also evaluated. In particular, a strategy based on a kinematic–dynamic formulation is proposed. Unlike other studies such as [22], the catenary is not explicitly included in the model, in order to improve robustness.
- The proposed formulation demonstrates that the contact force can be accurately estimated using acceleration and displacement measurements only at the center of the contact strips. The independence of the center dynamics with respect to force eccentricity provides an important simplification for practical implementation.

1.5. Layout

After this introduction, the theoretical foundations for the proposed method are included in Section 2. The general procedure for contact force estimation is explained in Section 3. The four different models employed for solving the inverse dynamic problem are detailed in Section 4 and the optimization of their hyperparameters in Section 5. Finally, the results obtained in the test bench are included in Section 6 and conclusions in Section 7.

2. Theoretical foundations

This paper proposes a method for estimating the contact force acting on a pantograph using the acceleration and displacement of the contact strip center and the pressure of the uplift system bellows.

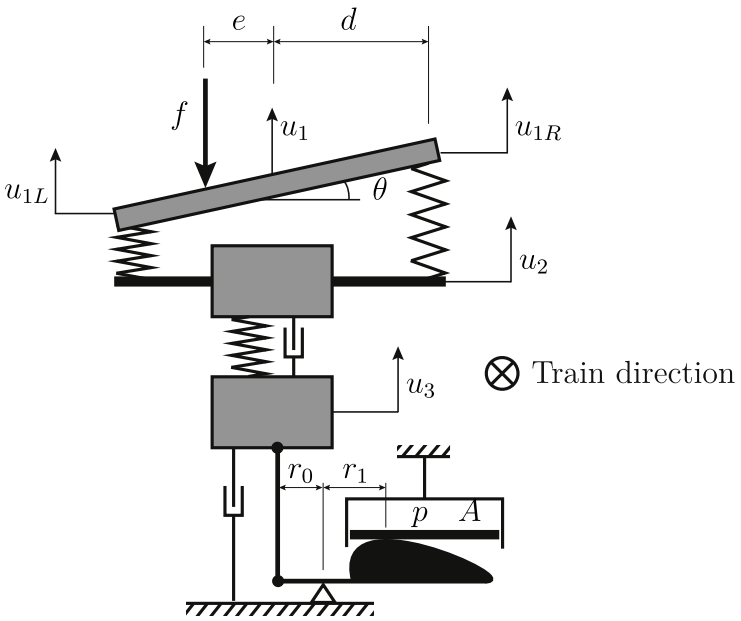


Fig. 1. Pantograph toy model.

Since the contact force acts at a varying position along the contact strip surface rather than at its center, it is necessary to assess whether its magnitude can be inferred from measurements acquired at the contact strip center. Furthermore, a methodology based on frequency separation is proposed to combine the information contained in pressure, acceleration, and displacement measurements for contact force estimation. The following subsections present the theoretical foundations that justify the proposed solution to these two issues.

2.1. Eccentric force

In a dynamic system, the motion induced by an applied force generally depends on the point of application of that force. However, for the motion of the pantograph contact strip center, this dependency is weak when the force is applied vertically at any point along the contact strips. The toy model shown in Fig. 1 is used to illustrate this property, which is subsequently validated experimentally in Section 6.3.1. In this model, the contact strips are represented by a rigid bar with mass m_1 and moment of inertia I_1, suspended by two springs of stiffness k separated by a distance $2d$. The bar can undergo a vertical displacement u_1 and a rotation θ. When a force is applied with an eccentricity e, the equations of motion associated with the degrees of freedom u_1 and θ are:

$$m_1\ddot{u}_1 + 2k\,u_1 = -f + 2k\,u_2 \tag{1}$$

$$I_1\ddot{\theta} + 2kd^2\,\theta = -f\,e \tag{2}$$

The equation governing u_1 is independent of e, indicating that the force produces the same motion at the contact strip center regardless of its point of application. In contrast, the force eccentricity generates a torque that induces rotation of the contact strips. Therefore, under this simplified model, the contact force can be inferred from the motion of the contact strip center independently of the force position.

2.2. Frequency separation

The mean value of the contact force cannot be inferred from the acceleration or the displacement of the contact strips. Instead, the mean value of the contact force is controlled by the pressure in the bellows of the pantograph uplift mechanism and can be estimated using the mean pressure. This inability of acceleration/displacement measurements to predict the mean value of the contact force can be extended to the very low-frequency range, where the behaviour of the pantograph can be considered quasi-static and the force might still be inferred from pressure.

After that, the remaining frequency content is inferred from acceleration or displacement measurements.

To explain the basis of this procedure, the toy model in Fig. 1 is used, and its validity and limitations are discussed with experimental tests in Section 6.3.2.

2.2.1. Very low frequency range

In the toy model, the bellows is included as a force proportional to the pressure p and the area A, applied on a cam mechanism, so the force transmitted to the third degree of freedom is $pA\,r_1/r_0$, where the ratio r_1/r_0 may be a function of u_3 (see Fig. 1). A cam

mechanism is present in the real pantograph and is designed to compensate for geometrical nonlinearities and achieve a constant mean force for different pantograph heights. Thus, a constant r_1/r_0 is assumed in the toy model, to be confirmed experimentally.

In the very low-frequency range, the pantograph is assumed to behave quasi-statically, i.e., inertia and damping forces are neglected. Thus, the contact force f depends on the pressure p, the contact strip height u_1, and the lateral eccentricity e. Since it has been shown that e only affects the θ dynamics (Eq. (1)) and that the cam mechanism reduces the dependence of the mean contact force on pantograph height, the force can be written as a function of pressure, $f = f(p)$, considering only the very low frequency of both signals. In this work, this function is assumed to be linear but it must be validated experimentally.

2.2.2. Higher frequency range

We assume that the bellows pressure is determined by the regulator reference value p_0 and by the displacement changes of the bellows. The pressure variations induced by the regulator are very slow, as confirmed experimentally, and therefore do not affect the higher-frequency content, where pressure changes are then produced exclusively by the pantograph motion. Consequently, pressure does not need to be treated as an external excitation, but rather as part of the model.

This allows us to infer the higher-frequency content of the contact force using only acceleration and displacement measurements, together with a pantograph model that includes the dynamic effects of the bellows. In most pantograph models, the bellows is represented as a spring acting on u_3.

2.2.3. Cut-off frequency

The cut-off frequency separating both methods must be defined by the user. The lower it is, the more accurate the quasi-static assumption becomes, and the smaller the error in the very low frequency estimation. The higher it is, the greater the sensitivity between acceleration and force, and the less likely it is that the high-frequency content is affected by pressure variations induced by the air regulator, resulting in a lower error in the higher frequency estimation. The cut-off frequency used in this work is selected by testing different values experimentally (see Section 6.3.3), and 0.5 Hz has been choosen.

3. Methodology

The scope of this work is the estimation of the contact force acting on a pantograph using a low-intrusive procedure, without structural modification of the pantograph, in order to simplify its implementation compared with the traditional contact force measurement method.

The methodology proposed is implemented and validated in a laboratory environment using a test rig (see Fig. 2) that is able to: (1) impose a desired displacement on the pantograph contact strips using a linear actuator and (2) measure the total contact force exerted by the actuator over the two contact strips. In addition to the test rig, the equipment mounted on the pantograph for contact force estimation consists of: (3) two acceleration sensors placed on the center of both contact strips, (4) a displacement sensor for measuring the contact strips displacement, and (5) a pressure sensor in the pneumatic uplift mechanism system. In general, all signals are low-pass filtered at 20 Hz.

The experimental setup is shown in Fig. 3, and it consists of a ®LINMOT PS10-70x240U linear magnetic actuator (1) with a maximum velocity of 5.4 m/s and a maximum force of 1650 N, driven by an E1450 motor controller (2) that receives position references via the EtherCAT protocol. A ®National Instruments CompactRIO cRIO-9040 real-time system (3) performs the main tasks of force, pressure, displacement, and acceleration acquisition using an NI 9234 (4), communication with the PC (5), and execution of the control loops. The main loop runs at 2 ms, acquiring measurements, while the motor control loop runs at 10 ms and updates the displacement commands sent to the actuator controller. Two ®Kyowa AS-5GA strain-gauge accelerometers (6) are used to measure the contact strip acceleration; both signals are averaged to obtain the acceleration at the center. The contact force is measured using two ®HBM U2B load cells (7) mounted on the actuator, with signal conditioning provided by AS1201 AC strain amplifiers (8). The pressure is measured with a 3100S sensor from ®Gems (9), and the displacement is measured directly at the actuator using an external linear encoder, the ®Linmot MS01-1/D-SSI (10). The pantograph used in this study is a DSA®380.03.

Since constant or very low-frequency forces do not, in practice, significantly affect acceleration or displacement signals, the estimation of the contact force is performed in two steps, separating the frequency content below and above 0.5 Hz. Following the scheme shown in Fig. 2, the low-frequency content of the contact force, $f^{\mathrm{Lo}}(t)$, is obtained from the pressure sensor of the bellow that lifts the pantograph. The sensor signal $p(t)$ is low-pass filtered at 0.5 Hz, after which a linear relationship is adopted:

$$f^{\mathrm{Lo}}(t) = c_0 + c_1\, p^{\mathrm{Lo}}(t) \tag{3}$$

where the coefficients c_0 and c_1 are determined through calibration.

Then, the high-frequency content of the contact force, $f^{\mathrm{Hi}}(t)$, is estimated using one of the four models described in Section 4, based on the vertical acceleration $a(t)$ and displacement $z(t)$ measured at the pantograph contact strip center. The resulting force component is high-pass filtered at 0.5 Hz.

Finally, the total estimated force is reconstructed as

$$f(t) = f^{\mathrm{Lo}}(t) + f^{\mathrm{Hi}}(t), \tag{4}$$

which can then be compared with the reference contact force $f^*(t)$ measured at the test bench (see point (2) in Fig. 2).

Using the described configuration of the test bench and measurement equipment, several tests have to be done to create a dataset. Every test is done imposing a pre-defined displacement signal at the contact strips of the pantograph. The dataset includes signals of

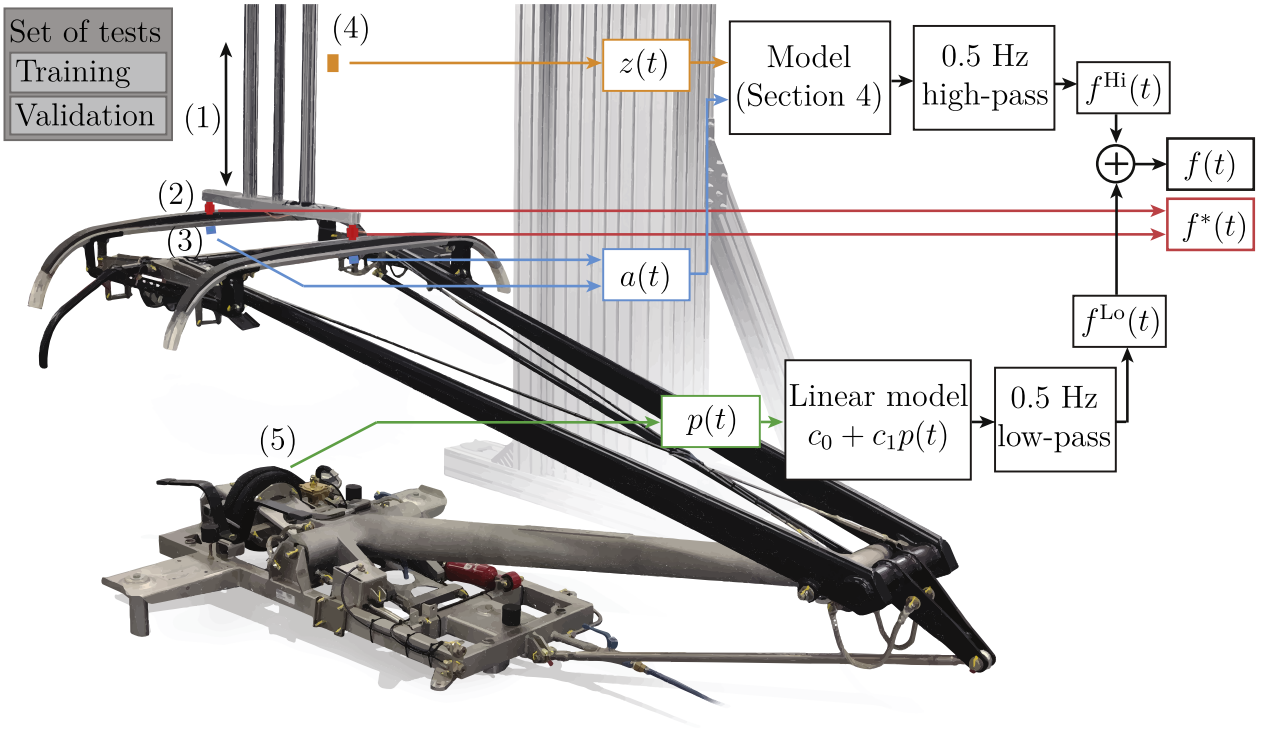


Fig. 2. Test bench and indirect measurement setup used for force estimation.

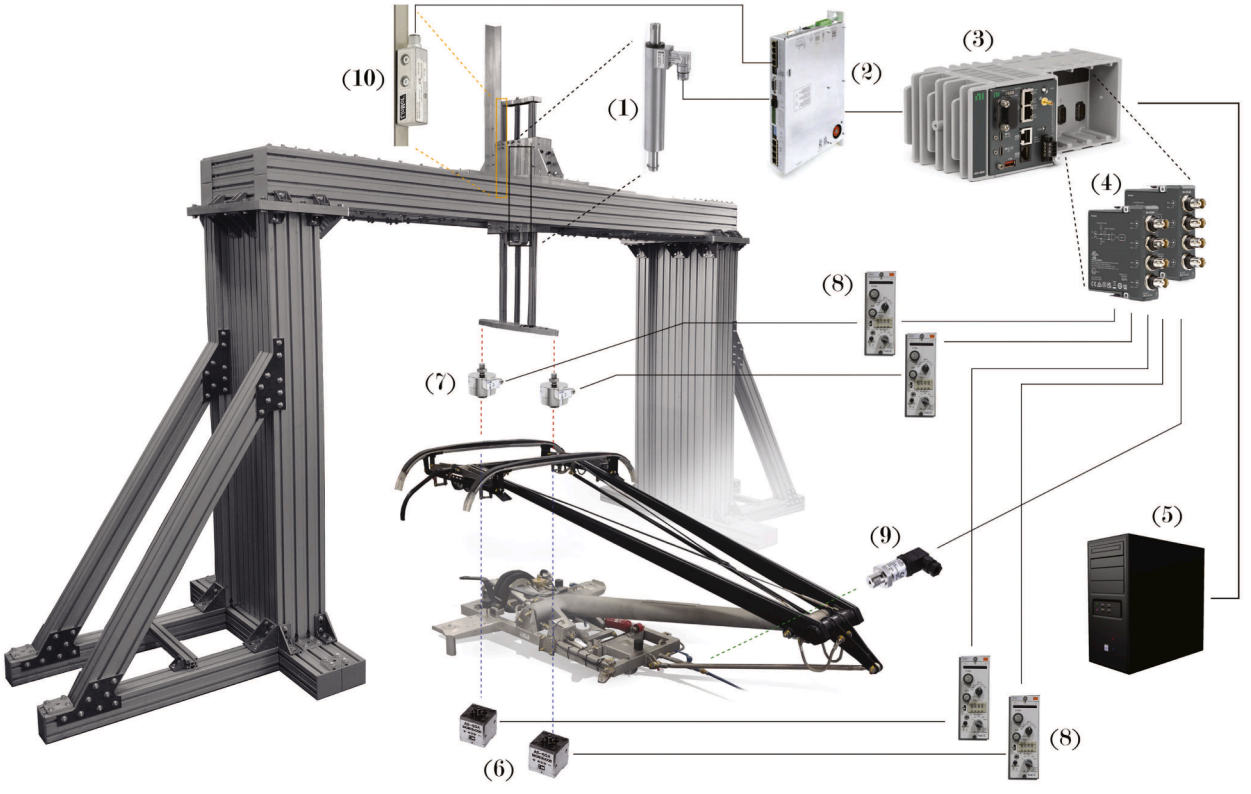


Fig. 3. Test bench setup.

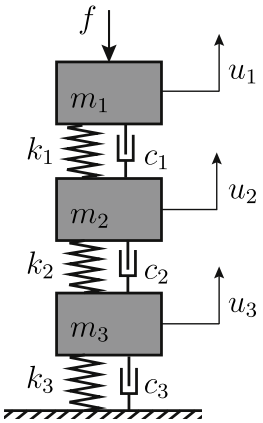


Fig. 4. Pantograph linear model.

acceleration, displacement, pressure and the actual force applied. The dataset is divided into two groups: training tests and validation tests. In Section 5, the parameters of the predictive models are optimized using the training set, and the performance of each optimized model is subsequently evaluated using the validation set.

The kinematics of the pantograph can be formulated such that it depends only on the pantograph model and the externally applied force. Including an explicit catenary model is an alternative approach; however, it is not considered in this work in order to improve robustness and ensure that the proposed method remains applicable to any type of catenary or, more generally, to any external excitation. Within this framework, the specific characteristics of the catenary or the source of excitation generating the force are not relevant to the estimation procedure.

4. Models

The methodology for CF estimation is explained in the previous section and summarised in Fig. 2, where the block called "model" is responsible for the prediction of the contact force in the 0.5–20 Hz range, $f^{\mathrm{Hi}}(t)$. This model is fed with the acceleration and displacement of the contact point (force application point) of the pantograph. Although in this Section we assume that both measurements are available, in Section 4.5 we will also consider that only acceleration is available. Four different models are tried out: (M1) Kalman Filter, (M2) Moving Horizon Estimator, (M3) Neural Network and (M4) LSTM.

4.1. M1: Augmented Kalman filter

The use of Kalman Filter is a classical approach for system state estimation [3] and its variant, the Augmented Kalman Filter (AKF), enables also the estimation of unknown inputs [4] by expanding the state space with those unknown inputs. Since it is a model-based approach, a pantograph model is needed. Here the broadly used [1] lumped-mass pantograph model of three degrees of freedom is adopted, consisting of mass, springs and dampers as shown in Fig. 4. Unlike in [22], only the pantograph is included in the model for the Kalman Filter, since the dependence of excitation force and measured variables can be determined only with the pantograph dynamics. The pantograph linear dynamic equation of motion can be written as:

$$\mathbf{M}\ddot{\mathbf{u}} + \mathbf{C}\dot{\mathbf{u}} + \mathbf{K}\mathbf{u} = \mathbf{S}f \tag{5}$$

where $\mathbf{M}$, $\mathbf{C}$, $\mathbf{K}$ are the mass, damping and stiffness matrices, $\mathbf{u}$ is the displacement of the three d.o.f, f is the unknown external force and $\mathbf{S}$ is the selection matrix for the force that in this case is $[-1, 0, 0]^{\top}$. This system can be transformed to a discrete time state-space representation, assuming for simplicity a zero order hold method, resulting for the time step $k+1$:

$$\mathbf{x}_{k+1} = \mathbf{F}\mathbf{x}_{k+1} + \mathbf{G}f_k + \mathbf{w}_k \tag{6}$$

where the state vector is:

$$\mathbf{x}_k = \begin{bmatrix} \dot{\mathbf{u}}_k \\ \mathbf{u}_k \end{bmatrix}; \tag{7}$$

$\mathbf{w}_k$ is the process noise that is assumed to be zero-mean Gaussian distributed with covariance matrix $\mathbf{Q}$; and $\mathbf{F}$ and $\mathbf{G}$ are the matrices resulting from the transformation. The system measurements variables can be defined, in general, as a linear combination of the state and inputs using matrices $\mathbf{H}$ and $\mathbf{J}$:

$$\mathbf{y}_k = \mathbf{H}\,\mathbf{x}_k + \mathbf{J}f_k + \mathbf{v}_k \tag{8}$$

where $\mathbf{v}_k$ is the measurement noise that is assumed to be zero mean gaussian distributed with covariance matrix $\mathbf{R}$.

The state extension can be done by including the external force as an additional state variable. In order to estimate the unknown force f_k, it is modeled as a gaussian process:

$$f_{k+1} = f_k + \eta_k \tag{9}$$

where η_k is a zero-mean Gaussian noise with variance Q_f that is the variance of the force increment $\Delta f = f_{k+1} - f_k$.

The augmented state vector is then defined as:

$$\mathbf{x}_k^\mathrm{a} = \begin{bmatrix} \dot{\mathbf{u}}_k \\ \mathbf{u}_k \\ f_k \end{bmatrix} \tag{10}$$

Using this augmented state vector, the discrete-time state-space model in Eq. (6) can be rewritten as:

$$\mathbf{x}_{k+1}^\mathrm{a} = \underbrace{\begin{bmatrix} \mathbf{F} & \mathbf{G} \\ \mathbf{0} & \mathbf{I} \end{bmatrix}}_{\mathbf{F}_\mathrm{a}} \mathbf{x}_k^\mathrm{a} + \begin{bmatrix} \mathbf{w}_k \\ \eta_k \end{bmatrix} \tag{11}$$

Similarly, Eq. (8) becomes:

$$\mathbf{y}_k = \underbrace{\begin{bmatrix} \mathbf{H} & \mathbf{J} \end{bmatrix}}_{\mathbf{H}_\mathrm{a}} \mathbf{x}_k^\mathrm{a} + \mathbf{v}_k \tag{12}$$

This augmented formulation allows the simultaneous estimation of the system states and the unknown external force by means of a standard KF applied to the augmented system.

4.1.1. M1.1: AKF with acceleration in the measurement

The measurements used for the force estimation are the displacement and acceleration of the contact point, that in the pantograph model correspond to u_1 and $\ddot{u}_1$. Thus the measured vector of Eq. (12) is $\mathbf{y} = [\ddot{u}_1 \;\; u_1]^\top$. In order to express the acceleration $\ddot{u}_1$ as a linear function of $\mathbf{x}$ and f it is necessary to use Eq. (5). To that end the desired measurement $\mathbf{y}$ can be written first as a function of displacement, velocity and acceleration of the d.o.f:

$$\mathbf{y} = \mathbf{S}_\mathrm{a}\ddot{\mathbf{u}} + \mathbf{S}_\mathrm{v}\dot{\mathbf{u}} + \mathbf{S}_\mathrm{d}\mathbf{u} \tag{13}$$

For this specific case measuring displacement and acceleration of the first d.o.f., the selection matrices are:

$$\mathbf{S}_\mathrm{a} = \begin{bmatrix} 1 & 0 & 0 \\ 0 & 0 & 0 \end{bmatrix}; \qquad \mathbf{S}_\mathrm{v} = \begin{bmatrix} 0 & 0 & 0 \\ 0 & 0 & 0 \end{bmatrix}; \qquad \mathbf{S}_\mathrm{d} = \begin{bmatrix} 0 & 0 & 0 \\ 1 & 0 & 0 \end{bmatrix} \tag{14}$$

Then, the matrices of Eq. (12) can be then written as:

$$\mathbf{H} = \begin{bmatrix} \mathbf{S}_\mathrm{v} - \mathbf{S}_\mathrm{a}\mathbf{M}^{-1}\mathbf{C} & \mathbf{S}_\mathrm{d} - \mathbf{S}_\mathrm{a}\mathbf{M}^{-1}\mathbf{K} \end{bmatrix}; \quad \mathbf{J} = \mathbf{S}_\mathrm{a}\mathbf{M}^{-1}\mathbf{S} \tag{15}$$

A standard KF can be used with the system defined by Eqs. (11) and (12) and the contact force can be retrieved from the state vector.

4.1.2. M1.2: AKF with coloured noise

In the previous approach the force is assumed to follow a Gaussian process as defined in Eq. (9) with white noise, but the noise could be coloured if η is built with white noise and a first-order filter:

$$\eta_{k+1} = A_\mathrm{f}\,\eta_k + \xi_k \tag{16}$$

where ξ_k is a zero-mean Gaussian noise with covariance Q_ξ.

This first-order filter is defined as a low-pass filter since the assumption is that the external force has as frequency content below ω_c. It can be defined as:

$$A_\mathrm{f} = \exp(-\omega_\mathrm{c}\,\Delta t) \tag{17}$$

In this scenario, the system state is further augmented as:

$$\underbrace{\begin{bmatrix} \mathbf{x}_{k+1} \\ f_{k+1} \\ \eta_{k+1} \end{bmatrix}}_{\mathbf{x}_{k+1}^\mathrm{a}} = \underbrace{\begin{bmatrix} \mathbf{F} & \mathbf{G} & \mathbf{0} \\ \mathbf{0} & 1 & 1 \\ \mathbf{0} & 0 & A_\mathrm{f} \end{bmatrix}}_{\mathbf{F}_\mathrm{a}} \underbrace{\begin{bmatrix} \mathbf{x}_k \\ f_k \\ \eta_k \end{bmatrix}}_{\mathbf{x}_k^\mathrm{a}} + \begin{bmatrix} \mathbf{w}_k \\ \mathbf{0} \\ \xi_k \end{bmatrix} \tag{18}$$

With this new state vector, Eq. (12) can be rewritten as:

$$\mathbf{y}_k = \underbrace{\begin{bmatrix} \mathbf{H} & \mathbf{J} & \mathbf{0} \end{bmatrix}}_{\mathbf{H}_\mathrm{a}} \mathbf{x}_k^\mathrm{a} + \mathbf{v}_k \tag{19}$$

where the expressions of Eq. (15) are still valid. Again a standard Kalman Filter can be used with the system defined by Eqs. (18) and (19) and the contact force can be retrieved from the state vector.

4.1.3. M1.3: AKF with acceleration input

In Section 4.1.1, the use of acceleration measurements within a Kalman filter framework has been introduced. In this section, a different strategy is presented, inspired by applications in transportation where position is estimated using both position (GPS) and acceleration measurements. In such approaches, acceleration is treated as an input to the filter while position measurements are used as outputs and kinematic equations (relating position, velocity and acceleration with derivatives) are used instead of dynamic equations.

Here we propose to use a mixed kinematic–dynamic formulation, some degrees of freedom are governed by the dynamic equation (Eq. (5)) and others can be related with acceleration by means of derivatives (kinematic formulation).

Acceleration measurements are available only for a subset of the degrees of freedom (d.o.f.'s), denoted as group a. These d.o.f.'s are described using kinematic equations while the remaining ones, denoted as group b, for which acceleration measurements are not available, are described using dynamic equations.

The displacement vector is partitioned as:

$$\mathbf{u} = \begin{bmatrix} \mathbf{u}_a \\ \mathbf{u}_b \end{bmatrix} \tag{20}$$

The dynamic equation of motion, Eq. (5), can divided as:

$$\begin{bmatrix} \mathbf{M}_{aa} & \mathbf{M}_{ab} \\ \mathbf{M}_{ba} & \mathbf{M}_{bb} \end{bmatrix} \begin{bmatrix} \ddot{\mathbf{u}}_a \\ \ddot{\mathbf{u}}_b \end{bmatrix} + \begin{bmatrix} \mathbf{C}_{aa} & \mathbf{C}_{ab} \\ \mathbf{C}_{ba} & \mathbf{C}_{bb} \end{bmatrix} \begin{bmatrix} \dot{\mathbf{u}}_a \\ \dot{\mathbf{u}}_b \end{bmatrix} + \begin{bmatrix} \mathbf{K}_{aa} & \mathbf{K}_{ab} \\ \mathbf{K}_{ba} & \mathbf{K}_{bb} \end{bmatrix} \begin{bmatrix} \mathbf{u}_a \\ \mathbf{u}_b \end{bmatrix} = \begin{bmatrix} \mathbf{f}_a \\ \mathbf{f}_b \end{bmatrix} \tag{21}$$

Only the second row of equations regarding the d.o.f $\mathbf{u}_b$ are used; for the d.o.f's in group a the dynamic equations are replaced by the kinematic state-space equations:

$$\begin{bmatrix} \ddot{\mathbf{u}}_a \\ \dot{\mathbf{u}}_a \end{bmatrix} = \begin{bmatrix} \mathbf{0} & \mathbf{0} \\ \mathbf{I} & \mathbf{0} \end{bmatrix} \begin{bmatrix} \dot{\mathbf{u}}_a \\ \mathbf{u}_a \end{bmatrix} + \begin{bmatrix} \mathbf{I} \\ \mathbf{0} \end{bmatrix} \mathbf{a}_a \tag{22}$$

where $\mathbf{a}_a$ is the acceleration (measurement treated as an input) of the a set of d.o.f's.

Combining the dynamic equations Eq. (21) for b and the kinematic ones Eq. (22) for a, the space-state continuous time representation is:

$$\begin{bmatrix} \ddot{\mathbf{u}}_a \\ \ddot{\mathbf{u}}_b \\ \dot{\mathbf{u}}_a \\ \dot{\mathbf{u}}_b \end{bmatrix} = \begin{bmatrix} \mathbf{0} & \mathbf{0} & \mathbf{0} & \mathbf{0} \\ -\mathbf{M}_{bb}^{-1}\mathbf{C}_{ba} & -\mathbf{M}_{bb}^{-1}\mathbf{C}_{bb} & -\mathbf{M}_{bb}^{-1}\mathbf{K}_{ba} & -\mathbf{M}_{bb}^{-1}\mathbf{K}_{bb} \\ \mathbf{I} & \mathbf{0} & \mathbf{0} & \mathbf{0} \\ \mathbf{0} & \mathbf{I} & \mathbf{0} & \mathbf{0} \end{bmatrix} \begin{bmatrix} \dot{\mathbf{u}}_a \\ \dot{\mathbf{u}}_b \\ \mathbf{u}_a \\ \mathbf{u}_b \end{bmatrix} + \begin{bmatrix} \mathbf{I} & \mathbf{0} \\ -\mathbf{M}_{bb}^{-1}\mathbf{M}_{ba} & \mathbf{I} \\ \mathbf{0} & \mathbf{0} \\ \mathbf{0} & \mathbf{0} \end{bmatrix} \begin{bmatrix} \mathbf{a}_a \\ \mathbf{f}_b \end{bmatrix} + \mathbf{w} \tag{23}$$

where the process noise is denoted by $\mathbf{w}$, assumed to be zero-mean Gaussian with covariance matrix $\mathbf{Q}$. In this work, the acceleration and displacement are available only for the d.o.f. number 1 so the a group includes d.o.f. 1 and group b the other ones. The external forces on b d.o.f. are supposed to be null.

The system output may be defined as the displacement of the d.o.f's in group a (in this work for d.o.f number 1):

$$\mathbf{y} = \mathbf{u}_a + \mathbf{v} \tag{24}$$

where $\mathbf{v}$ is the measurement noise, assumed to be zero-mean Gaussian with covariance matrix $\mathbf{R}$.

The Kalman filter is implemented by using the measured acceleration of d.o.f 1 as an input to the system model, while the measured displacement is used as the measurement for the correction step.

After estimating the state of the system defined by Eqs. (23) and (24) with a standard Kalman Filter, the external force applied to the d.o.f.'s in group a (the contact force) can be obtained in a post-processing step using Eq. (21):

$$\mathbf{f}_a = \mathbf{M}_{aa}\ddot{\mathbf{u}}_a + \mathbf{C}_{aa}\dot{\mathbf{u}}_a + \mathbf{K}_{aa}\mathbf{u}_a + \mathbf{M}_{ab}\ddot{\mathbf{u}}_b + \mathbf{C}_{ab}\dot{\mathbf{u}}_b + \mathbf{K}_{ab}\mathbf{u}_b \tag{25}$$

where the acceleration of the d.o.f's in group b is obtained from:

$$\ddot{\mathbf{u}}_b = \mathbf{M}_{bb}^{-1}\left(\mathbf{f}_b - \mathbf{C}_{bb}\dot{\mathbf{u}}_b - \mathbf{K}_{bb}\mathbf{u}_b - \mathbf{M}_{ba}\mathbf{a}_a - \mathbf{C}_{ba}\dot{\mathbf{u}}_a - \mathbf{K}_{ba}\mathbf{u}_a\right) \tag{26}$$

4.2. M2: Moving horizon estimator

The second model used for indirect contact force measurement is based on a Moving Horizon Estimator [32] (MHE) for systems with unknown input [33]. As the KF, it works by minimizing the difference between measured and predicted system outputs.

The pantograph dynamics, described by Eq. (5), can be transformed to a discrete-time linear state-space model (Eq. (6)), but in this case the state vector includes displacement, velocity, and acceleration:

$$\mathbf{x}_k = \begin{bmatrix} \ddot{\mathbf{u}}_k \\ \dot{\mathbf{u}}_k \\ \mathbf{u}_k \end{bmatrix} \tag{27}$$

Given a time step k, the system dynamics over a finite horizon of N_{H} time steps can be written in compact form as:

$$\bar{\mathbf{x}} = \bar{\mathbf{F}}\mathbf{x}_k + \bar{\mathbf{G}}\bar{\mathbf{f}}, \tag{28}$$

where the state and force vectors are augmented for the entire horizon:

$$\bar{\mathbf{x}} = \begin{bmatrix} \mathbf{x}_{k+1} \\ \dots \\ \mathbf{x}_{k+N_H} \end{bmatrix}; \quad \bar{\mathbf{f}} = \begin{bmatrix} f_{k+1} \\ \dots \\ f_{k+N_H} \end{bmatrix} \tag{29}$$

and the matrices $\mathbf{F}$ and $\mathbf{G}$ are augmented to compute N_H consecutive steps:

$$\bar{\mathbf{F}} = \begin{bmatrix} \mathbf{F} \\ \mathbf{F}^2 \\ \mathbf{F}^3 \\ \dots \\ \mathbf{F}^{N_H-1} \end{bmatrix}; \quad \bar{\mathbf{G}} = \begin{bmatrix} \mathbf{G} & 0 & 0 & \dots & 0 \\ \mathbf{FG} & \mathbf{G} & 0 & \dots & 0 \\ \mathbf{F}^2\mathbf{G} & \mathbf{FG} & \mathbf{G} & \dots & 0 \\ \dots & \dots & \dots & \dots & \dots \\ \mathbf{F}^{N_H-2}\mathbf{G} & \mathbf{F}^{N_H-3}\mathbf{G} & \mathbf{F}^{N_H-4}\mathbf{G} & \dots & \mathbf{G} \end{bmatrix} \tag{30}$$

Only a subset of the state is available through measurements. The measured outputs are related to the state vector by:

$$\mathbf{y}_k = \mathbf{H}\mathbf{x}_k, \tag{31}$$

where the matrix $\mathbf{H}$ selects the measured position and acceleration o the first d.o.f (pantograph head) using the selection matrices defined in Eq. (14):

$$\mathbf{H} = \begin{bmatrix} \mathbf{S}_a & \mathbf{S}_v & \mathbf{S}_d \end{bmatrix} \tag{32}$$

To evaluate the prediction error over the considered horizon, the output equation is augmented following the same principle:

$$\bar{\mathbf{y}} = \bar{\mathbf{H}}\bar{\mathbf{x}}, \tag{33}$$

The external force is found by solving an optimization problem that minimises differences between model response and measurements and also variations between consecutive force samples are penalised in order to limit spurious oscillations of the predicted force. The external force is estimated by solving the following quadratic optimization problem:

$$\min_{\bar{\mathbf{f}}} \ (\bar{\mathbf{y}} - \bar{\mathbf{y}}^*)^\top \mathbf{S}(\bar{\mathbf{y}} - \bar{\mathbf{y}}^*) + \bar{\mathbf{f}}^\top \mathbf{P}\bar{\mathbf{f}} \tag{34}$$

subject to the system dynamics defined in Eqs. (28) and (33). The reference output vector $\bar{\mathbf{y}}^*$ is constructed from the measured position and acceleration signals over the horizon. Diagonal matrix $\mathbf{S}$ serves to penalise the difference between the system predicted response and the measured one, weighted with different coefficients k_u and k_a for displacement and acceleration measurements, respectively:

$$\mathbf{S} = \begin{bmatrix} k_a & 0 & 0 & 0 & \cdots & 0 \\ 0 & k_u & 0 & 0 & \cdots & 0 \\ 0 & 0 & k_a & 0 & \cdots & 0 \\ 0 & 0 & 0 & k_u & \cdots & 0 \\ \vdots & \vdots & \vdots & \vdots & \ddots & \vdots \\ 0 & 0 & 0 & 0 & \cdots & k_u \end{bmatrix} \tag{35}$$

On the other hand, matrix $\mathbf{P}$ penalises the variance of the contact force increment, weighted with the coefficient k_f:

$$\mathbf{P} = k_f \begin{bmatrix} 1 & -1 & 0 & 0 & \cdots & 0 \\ -1 & 2 & -1 & 0 & \cdots & 0 \\ 0 & -1 & 2 & -1 & \cdots & 0 \\ \vdots & \vdots & \vdots & \vdots & \ddots & -1 \\ 0 & 0 & 0 & 0 & -1 & 2 \end{bmatrix} \tag{36}$$

By substituting Eqs. (28) and (33) in Eq. (34) and enforcing the derivative of the cost function with respect to $\bar{\mathbf{f}}$ to be zero, the following linear system of equations is obtained:

$$(\bar{\mathbf{G}}^\top \bar{\mathbf{H}}^\top \mathbf{S}\bar{\mathbf{H}}\bar{\mathbf{G}} + \mathbf{P})\bar{\mathbf{f}} = \bar{\mathbf{G}}^\top \bar{\mathbf{H}}^\top \mathbf{S}\bar{\mathbf{y}}^* - \bar{\mathbf{G}}^\top \bar{\mathbf{H}}^\top \mathbf{S}\bar{\mathbf{H}}\bar{\mathbf{F}}\mathbf{x}_k \tag{37}$$

Solving this system provides the estimated sequence of external forces over the prediction horizon $\bar{\mathbf{f}}$. At each time step, the estimation window is advanced by $N_F < N_H$ steps, and predictions corresponding to overlapping intervals are crossfaded to obtain a single, consistent force estimate.

4.3. M3: Feedforward neural network

As shown in Fig. 5, a feedforward neural network regression model can be trained to predict the force at the kth time step with the input feature vector formed by the displacement z and acceleration a for the interval $[k - N_b, k + N_a]$, where N_b and N_a are the number of steps before and after the current one considered as output of the NN. The model was implemented using MATLAB's `fitrnet` function for regression. All input features are standardized to zero mean and unit variance prior to training in order to improve numerical stability and convergence behaviour.

The network architecture consists of fully connected hidden layers. Rectified Linear Unit (ReLU) activation functions are used after every hidden layer due to their ability to mitigate vanishing gradient effects and non-linearity. The output layer is linear,

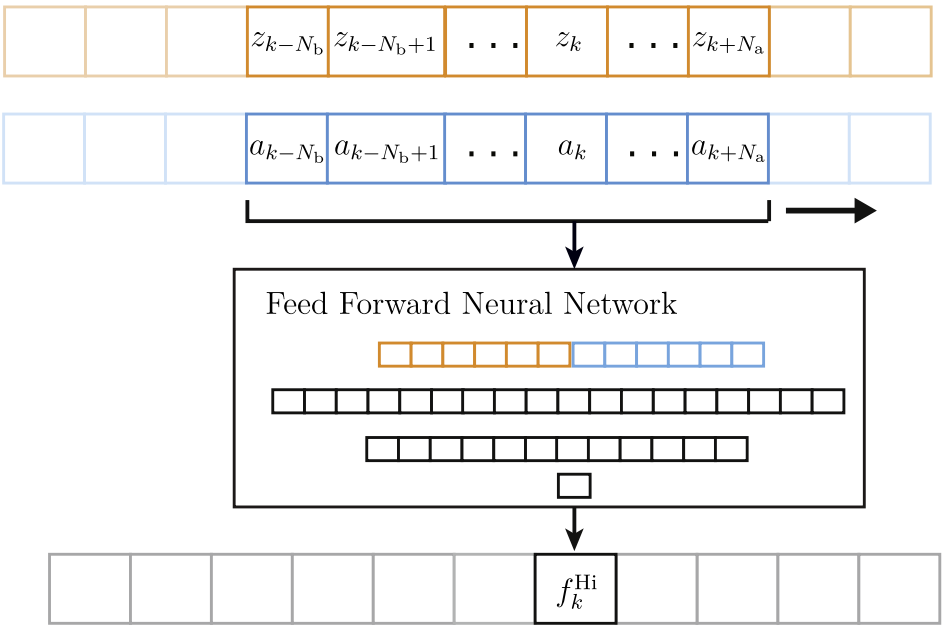


Fig. 5. M3 model for contact force prediction.

as appropriate for regression tasks. No cross-validation is employed during training. Model weights and biases were estimated by minimizing the regularized mean squared error loss function. The same network is applied sequentially for predicting all time steps performing as a sliding window (see Fig. 5).

Training is stopped either when a maximum of iterations is reached, the norm of the gradient falls below a threshold of 0.02, or the relative improvement in the loss function drops below 10%.

4.4. M4: Long-short term memory network

A recurrent neural network based on Long Short-Term Memory (LSTM) units is developed to model the non-linear relationship between the system kinematic measurements and the applied force. The network performs *sequence-to-sequence regression*, where time histories of displacement and acceleration are mapped to a time history of force.

Each training sample consists of a multivariate time sequence:

$$\mathbf{X} = \begin{bmatrix} z(t_1) & z(t_2) & \dots & z(t_T) \\ a(t_1) & a(t_2) & \dots & a(t_T) \end{bmatrix} \tag{38}$$

where $z(t)$ and $a(t)$ denote displacement and acceleration, respectively, and T is the sequence length. The target output is the force sequence

$$\mathbf{Y} = \begin{bmatrix} f(t_1) & f(t_2) & \dots & f(t_T) \end{bmatrix}. \tag{39}$$

To improve training stability, feature-wise normalization was applied using statistics (standard deviation and average) computed from the training set only.

$$\tilde{\mathbf{X}} = \frac{\mathbf{X} - \boldsymbol{\mu}^{(X)}}{\boldsymbol{\sigma}^{(X)}}; \qquad \tilde{\mathbf{Y}} = \frac{\mathbf{Y} - \boldsymbol{\mu}^{(Y)}}{\boldsymbol{\sigma}^{(Y)}}. \tag{40}$$

The inverse transformation is carried out on the net prediction results.

The neural network architecture is implemented in MATLAB® composed of the following layers: a **sequence input layer** with 2 features (displacement and acceleration) and no internal normalization, a single LSTM layer with N_S hidden units, a fully connected layer mapping the hidden state to the output dimension of one and a regression layer computing the mean squared error loss. The LSTM layer operates in sequence output mode, producing one output per time step.

Training was performed using the Adam optimizer. The loss function is the mean squared error (MSE) between predicted and normalized force sequences. To enhance numerical stability, gradient clipping was applied with a threshold of 1. The model was trained for a maximum number of epochs and an early stopping strategy based on training loss was applied. Training was terminated if the loss did not improve by at least a fixed tolerance over a predefined number of consecutive epochs (patience criterion).

Table 1
Optimised parameters in every model.

M1 (AKF)	M2 (MHE)	M3 (NN)	M4 (LSTM)
k_1, k_2, k_3	k_1, k_2, k_3	N_b	Size 1
c_1, c_2, c_3	c_1, c_2, c_3	Size 1	
m_1, m_2, m_3	m_1, m_2, m_3	Size 2	
ω_c (Only for M1.2)	k_a, k_u, k_f		
Q_v, Q_z, R_a, R_z			

4.5. Problem 1 and problem 2

As seen in Fig. 2, displacement $z(t)$ and acceleration $a(t)$ are available in the test setup but the necessity of using the displacement signal is analysed in this work. Thus, we define Problem 1 in which $z(t)$ and $a(t)$ are available and Problem 2 in which only $a(t)$ is used as input.

In Problem 2, the displacement measurement is unavailable and the contact vector state exhibits a slow drift, as observed during implementation of model-based estimation frameworks such as the Kalman Filter (KF) and Moving Horizon Estimation (MHE).

To address this, the strategy consists on including all the information that is known about the displacement: it is zero, with an uncertainty equal to an estimate of its standard deviation. Thus, the displacement is set to $z(t) = 0$ in the measurement vector and the uncertainty is set to a higher value respect to the case with displacement measurement. Its important to remark that this does not imply that the estimator interprets the displacement as physically zero. In the AKF/MHE formulation, the measurement update is weighted by the inverse of the covariance matrix $\mathbf{R}$, so increasing the variance associated with $z(t)$ effectively reduces its influence on the state correction step.

In contrast, data-driven approaches do not exhibit this issue because the mapping from measurements to force is learned directly from data and does not rely on recursive state propagation.

5. Parameter optimization

The four models defined in Section 4 have several user-define parameters. In this Section define how they have been determined to assure a good representation of the model potential and a fair comparison between them.

5.1. Non-optimised parameters

In KF models, the process noise of the contact force is the variance of the contact force increment. In pantograph-catenary interaction, the acceleration of upper mass of the pantograph model, m_1, is responsible for most of the contact force and the variance of $m_1 a(t)$ is a good estimation of the contact force variance. Assuming initially that $f = m_1 a$, the process noise of the contact force can be determined as:

$$Q_f = \mathrm{Var}(\eta_k), \quad \text{where } \eta_k = f_{k+1} - f_k. \tag{41}$$

For the colour noise KF (M1.2) it can be estimated as:

$$Q_\eta = \mathrm{Var}(\xi_k), \quad \text{where } \xi_k = \eta_{k+1} - A_f \eta_k = f_{k+2} - f_{k+1} - A_f(f_{k+1} - f_k). \tag{42}$$

In MHE models, the results are not very sensitive to the horizon N_H and the overlapping window N_F if they are sufficiently large, so values of 300 and 20 time steps, respectively are used in this work.

NN models are applied convolutionally including a window of time. The number of steps after the current one, N_a, has shown little significance, so a value of $N_a = 5$ time steps is used.

5.2. Optimised parameters

All the parameters that are being optimised are gathered in Table 1. For M1, the pantograph model coefficients, the cut frequency ω_c and noise covariances matrices. To reduce the amount of parameters to define the KF models, the process and measurement noise covariance matrices, $\mathbf{Q}$ and $\mathbf{R}$, are assumed to be diagonal (no cross-correlation between disturbances) and the same for each d.o.f:

$$\mathbf{Q} = \begin{bmatrix} Q_v \mathbf{I}_3 & \mathbf{0} \\ \mathbf{0} & Q_u \mathbf{I}_3 \end{bmatrix}; \quad \mathbf{R} = \begin{bmatrix} R_a & 0 \\ 0 & R_z \end{bmatrix} \tag{43}$$

where Q_v, Q_u, R_a and R_z are the noise variances of the velocity, position, acceleration measured and displacement measured, respectively, that have to be optimised. For M2, the pantograph model coefficients and the penalising constants k_a, k_u and k_f. For M3, the number of previous steps N_b for feeding the NN and the sizes of the two layers. Finally, for M4, only the size (number of hidden units) of the LSTM network.

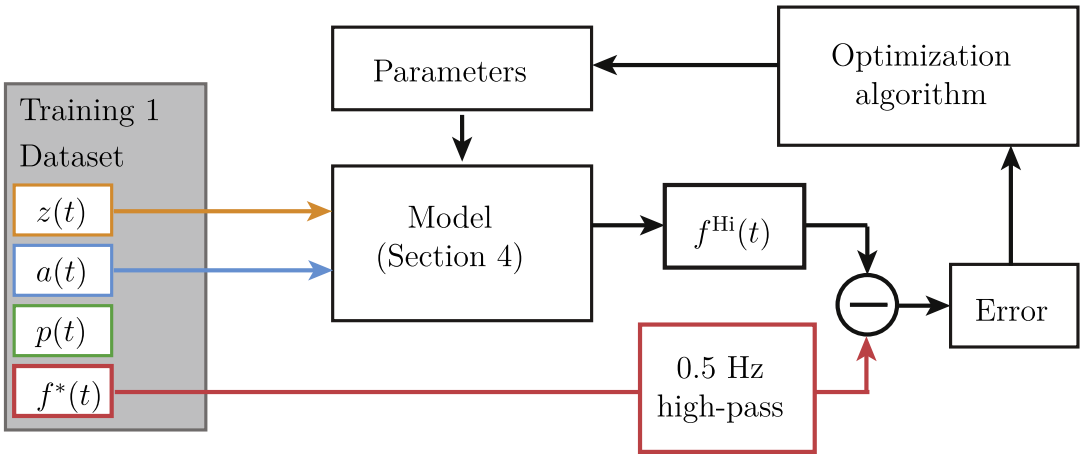


Fig. 6. Parameter optimization scheme for model-based models (M1 and M2).

5.3. Optimisation and training strategy

Depending on whether the model is model-based (M1–M2) or data-driven (M3–M4), two different optimization schemes are adopted as seen in Figs. 6 and 7, respectively. The optimisation is performed independently for Problem 1 and Problem 2. The training dataset is divided into two subsets, Training 1 and Training 2, so the data-driven models can be both, trained (computation of weighs and biases) and optimised (computation of optimal values of the parameters). Validation dataset is not used in the optimisation process.

Model-based models (M1–M2). In this case only the first training dataset is required. The model output is compared with the measured contact force (after subtracting the frequency content below 0.5 Hz) and their difference is used to compute the error. An optimization algorithm iteratively adjusts the model parameters to reduce this error.

Data-driven models (M3–M4). In the data-driven models optimisation, the model needs to be trained, and this is done with the Training 1 dataset, resulting in a trained model. This training loop is inside an outer loop to optimise the parameters. The training is done every evaluation of the objective function of the optimisation algorithm. The error is computed with the Training 2 dataset instead of Training 1 dataset because otherwise the error will always decrease when increasing the network size, leading to overfitting.

5.4. Optimisation algorithm

As the number of parameters and evaluation time are very different for model-based and data-driven models, also different optimization strategies are used. Parallel evaluations are employed, and stopping criterium are based on the lack of significant improvement over a large number of evaluations, ensuring efficient yet thorough search of the parameter space. The search range is defined with a lower bound set to one fifth of the initial values and an upper bound set to five times the initial values. Initial values are provided in Section 6.2.

Model-based models (M1–M2). The parameters of the M1 and M2 are optimised using a Genetic Algorithm (GA). This population-based global optimization method is selected because the evaluation of the objective function requires little computational cost and the number of parameters is high. The GA starts from an initial population centered around a nominal parameter vector which evolves over multiple generations through selection and variation mechanisms. Parameter bounds are enforced, and parallel computation is used to accelerate the process. The optimization runs for a large number of generations to ensure convergence toward a global or near-global minimum of the force prediction error.

Data-driven models (M3–M4). For the data-driven approach, hyperparameters are tuned using Bayesian optimization. This method builds a probabilistic surrogate model of the objective function and uses it to balance exploration of the parameter space with exploitation of promising regions. Both continuous and integer parameters can be handled within predefined bounds. The algorithm is initialized around a nominal parameter set and iteratively selects new evaluation points to minimize the prediction error.

6. Results

This section first presents the displacement signals used for the tests included in the dataset, and then, a comparison, after optimisation, of the different models proposed. Finally, additional tests are analysed to check that the prediction of the low and high frequency content of the contact force can be used in a wide range of conditions.

6.1. Dataset

We imposed three different types of displacement signals on the pantograph to carry out the tests included in the dataset:

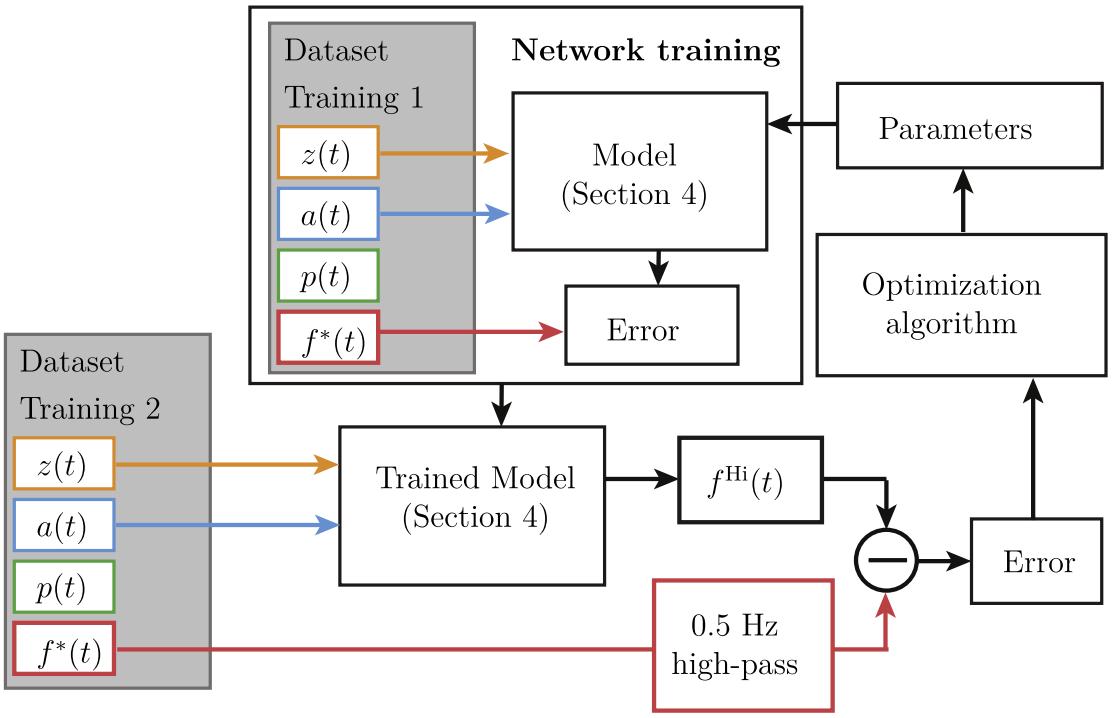


Fig. 7. Parameter optimization scheme for data-driven models (M3 and M4).

Table 2
Definition of the signal type, parameters and duration of the different tests and datasets.

Test	Signal Type	Parameter	T
1	Chirp $z(t) = A\left(1 - \frac{t}{T}\right)\sin\left(20\pi\frac{t}{T}\right)$	$A = 2$ mm	10 s
2		$A = 3$ mm	10 s
3		$A = 4$ mm	10 s
4	Pseudo $z(t) = \sum_{n=1}^{40} A\sin\left(\pi\, n\, t + \phi_{\mathrm{Rand}}\right)$	$\max(z) = 1.5$ mm	10 s
5		$\max(z) = 2.0$ mm	10 s
6		$\max(z) = 2.5$ mm	10 s
7	Catenary $z(t)$ from FEM simulation	225 km/h	10 s
8		250 km/h	10 s
9		275 km/h	10 s
10		300 km/h	10 s

Training 1
Training 2
Validation

- Chirp signals: the frequency linearly increases until 20 Hz with time while the amplitude is reduced also linearly.
- Pseudo signals: superposition of harmonic functions between 0 and 20 Hz with random phases.
- Catenary signals: displacement of the contact point of the contact wire from a simulated pantograph-catenary dynamic interaction at different train speeds.

All the tests performed are summarised in Table 2. The tests measurements are included either in the training dataset 1 or 2; or in the validation dataset. The last only includes catenary signals since they are the most similar to those faced in real pantograph operation. All measurements are acquired at a sampling rate of 2 ms.

Table 3
Initial parameter values used in the optimization process for M1.

Parameter	Value	Parameter	Value
k_1	11427 N/m	c_1	0.20 Ns/m
k_2	11544 N/m	c_2	5.73 Ns/m
k_3	207 N/m	c_3	5.85 Ns/m
m_1	7.39 kg	Q_z	8×10^{-9} m
m_2	7.01 kg	Q_v	1.2×10^{-3} m/s
m_3	3.82 kg	R_z	1.7×10^{-8} m
ω_c	$2 \times 20\pi$ rad/s	R_a	2.2×10^{-4} m/s^2

Table 4
Initial parameter values used in the optimization process for M2.

Parameter	Value	Parameter	Value
k_1	11427 N/m	c_1	0.20 Ns/m
k_2	11544 N/m	c_2	5.73 Ns/m
k_3	207 kg N/m	c_3	5.85 Ns/m
m_1	7.39 kg	K_u	2.6×10^{-1} m^{-2}
m_2	7.01 kg	K_a	4.6×10^{-3} s^{4}m^{-2}
m_3	3.82 kg	K_f	1.79×10^{-4} N^{-2}

Table 5
Initial parameter values used in the optimization process for M3 and M4.

M3 (NN)		M4 (LSTM)	
Parameter	Value	Parameter	Value
N_b	200	Size 1	40
Size 1	500		
Size 2	250		

6.2. Optimisation results and model comparison

To compare the models in terms of their ability to predict the contact force, the Normalized Mean Square Error (NMSE) is used as the performance metric. For a given individual test:

$$\mathrm{NMSE} = \frac{\sum_{k=1}^{N}(f_k - f_k^*)^2}{\sum_{k=1}^{N}(f_k^* - \bar{f}^*)^2} \tag{44}$$

where $\bar{f}^*$ is the mean of the measured force, f_k and f_k^* are the predicted and measured force at kth time instant of a total of N. When several tests are considered, the average of NMSE of all the tests included in every dataset is used.

The initial parameter values used in the optimization process are reported in Tables 3, 4, and 5. These values were selected by the authors based on prior experience with pantograph modelling and force estimation, as well as through a trial-and-error process aimed at obtaining stable convergence and satisfactory model performance. The optimization procedure was subsequently allowed to explore a broad range around these initial values (within a range from one fifth to five times the initial value).

The optimization process took an average computation time of 6 hours for the Kalman filter models and about 24 hours for the MHE and data-driven models on an Intel®Core™ i9, 3.6GHz, eight cores and 64GB RAM PC high-speed processor. The error was reduced an average of 97% in Kalman filter models, 83% in MHE model, 12% in NN model and 80% in LSTM model, but this reduction depends on the initialisation.

First, we compare the performance of the three different Kalman Filter models in Fig. 8 and then, the best of these three is compared with the remaining models in Fig. 9. In both figures the NMSE for different models and also for the two different problems (Problem 1 with acceleration and displacement measurements and Problem 2 with only acceleration) is shown. Also, the error for the training dataset tests and for the validation dataset tests can be differentiated. Between the KF models (M1 group), M1.1 and M1.2 are very similar and M1.3 (AKF with acceleration as an input) is the best and it is compared thus with the others models. Looking at Fig. 9 it can be concluded that NN and LSTM present the lowest error and similar performances although the differences with the AKF model are not greater. An important conclusion is that there is no increase of error in the Problem 2 respect to Problem 1 so this methodology could be applied with only the acceleration measurement without compromising performance.

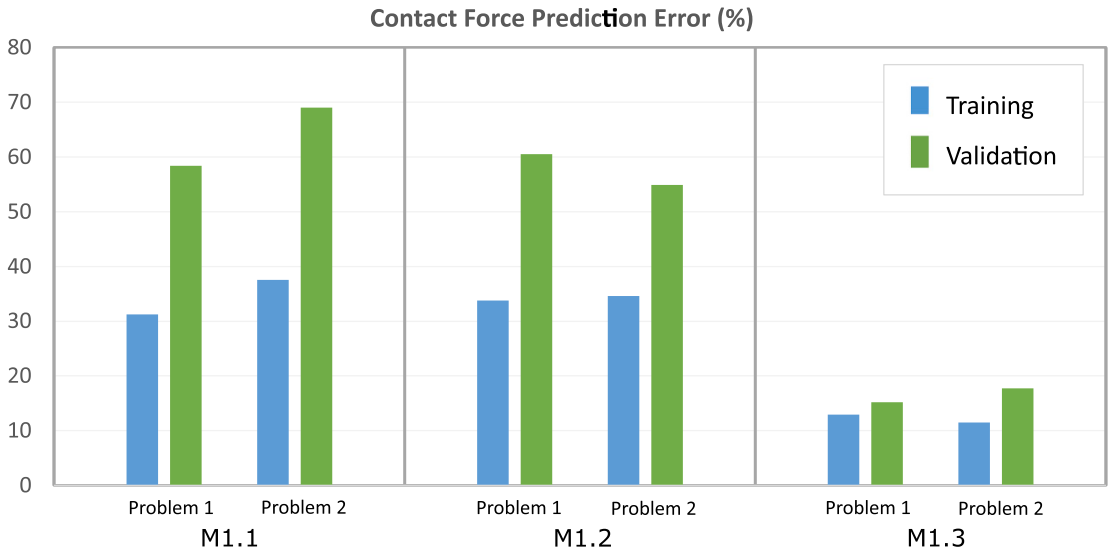


Fig. 8. Comparison of the contact force prediction error (NMSE) for the three different KF strategies.

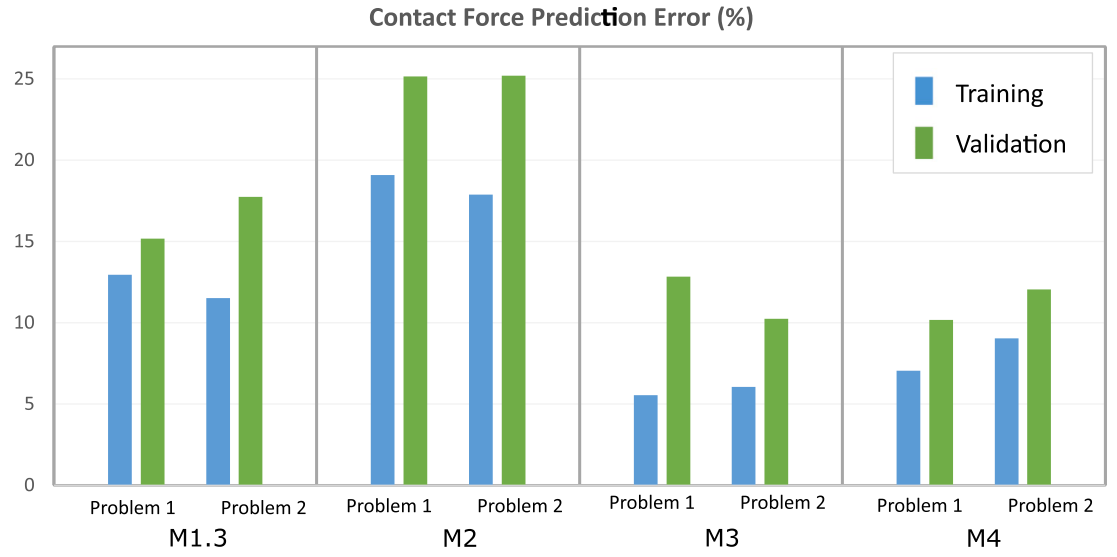


Fig. 9. Comparison of the contact force prediction error (NMSE) for the four models proposed.

The temporal representations of the predicted and measured forces in a section of every test of the validation dataset can be seen in Figs. 10–13 for the Problem 2 with AKF, Problem 1 with MHE, Problem 2 with NN and Problem 1 with LSTM, respectively. Looking at the figures, it can be observed that the results are better for the NN and LSTM models as indicated in Fig. 9. Also a comparison in the frequency domain for the Problem 1 with LSTM model is shown in Fig. 14.

6.3. Results analysis under different conditions

The optimisation process and model comparison have been carried out using the NMSE. However, other performance metrics, including MAE, RMSE, the correlation coefficient ρ, and the minimum, maximum, and standard deviation values, are also analysed in this section.

The tests used for model optimisation (Table 2) were conducted under specific conditions: the contact force was applied at the center of the contact strips, no regulator-induced pressure variations were present, the pantograph was set at a reference height, and

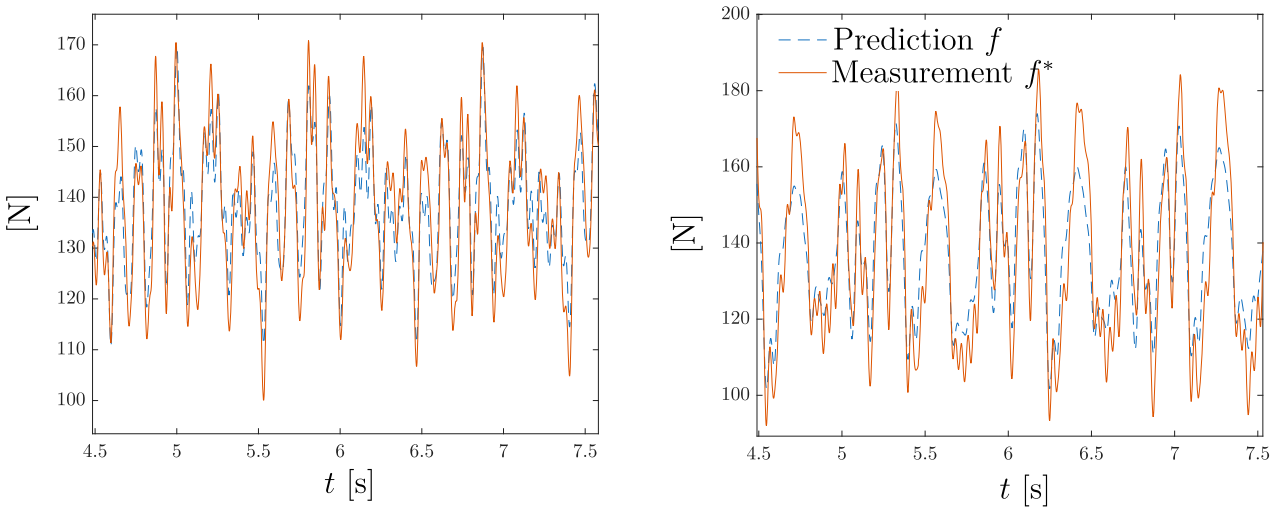


Fig. 10. M1.3 validation results of Problem 2: Catenary signals at 250 km/h (left) and 275 km/h (right).

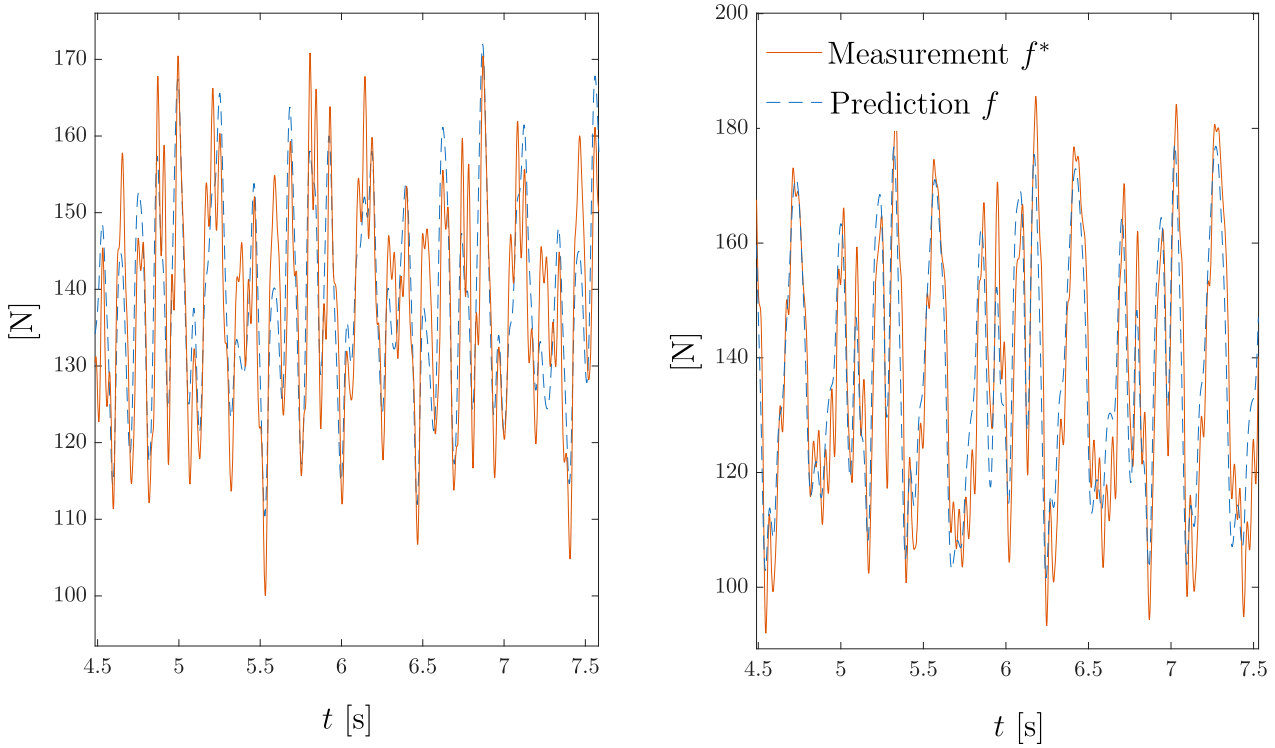


Fig. 11. M2 validation results of Problem 1: Catenary signals at 250 km/h (left) and 275 km/h (right).

the catenary excitation did not include any slope. Additional tests incorporating these effects are therefore considered to assess the validity and limitations of the proposed method.

Without loss of generality, model M4 and the Problem 2 configuration are used in this section to predict the high-frequency content of the contact force. The minimum, maximum, and standard deviation of both the measured and predicted contact forces for the tests with catenary signals at 250 and 275 km/h (Tests 8 and 9 in Table 2) are reported in Table 6. It can be observed that the predicted contact force exhibits a larger range and standard deviation than the measured force, although the differences remain within reasonable limits. The MAE, RMSE, NMSE, and ρ values for the same tests are presented in Table 7. Both tables show a slightly larger prediction error for the 275 km/h test.

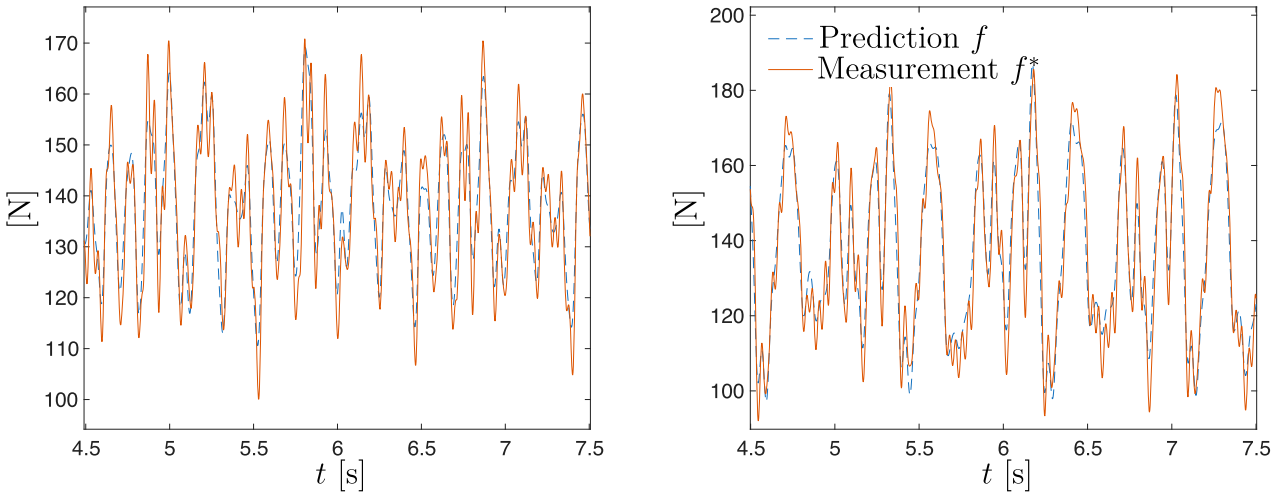


Fig. 12. M3 validation results of Problem 2: Catenary signals at 250 km/h (left) and 275 km/h (right).

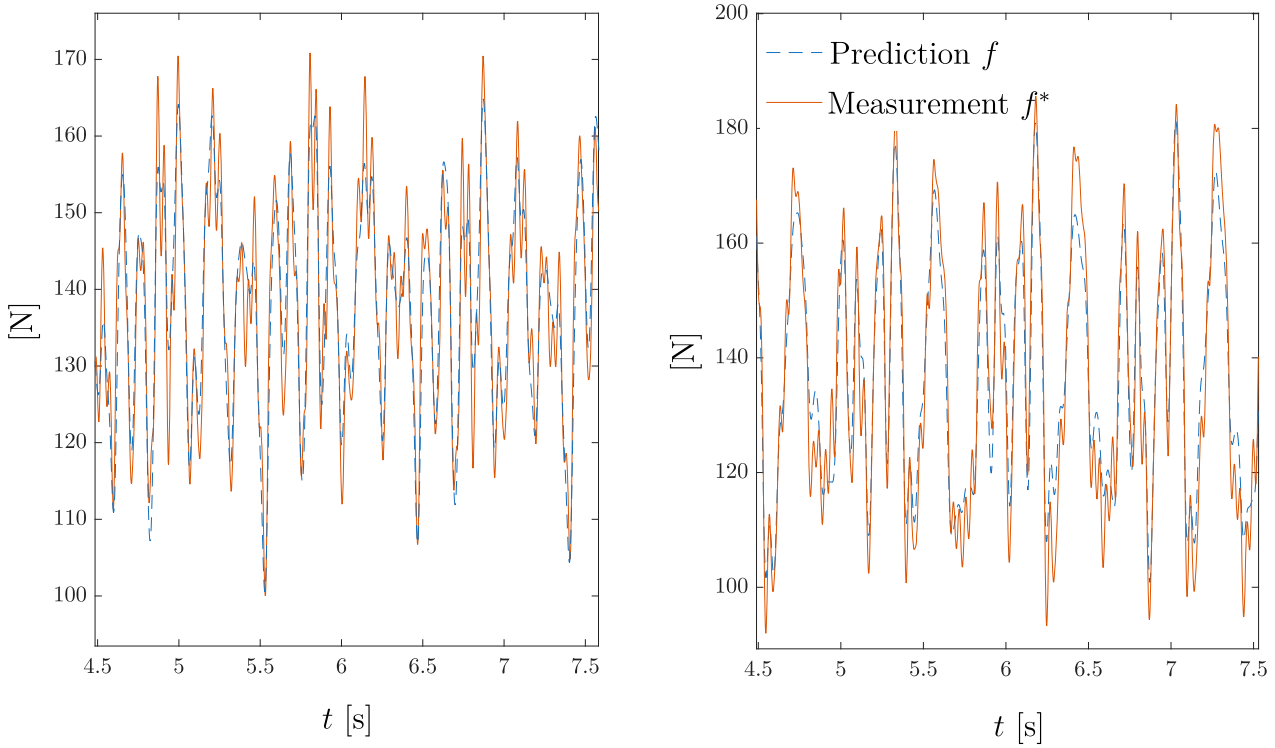


Fig. 13. M4 validation results of Problem 1: Catenary signals at 250 km/h (left) and 275 km/h (right).

Table 6
Descriptive statistics of the measured and predicted contact force for tests with catenary signals at 250 and 275 km/h (test 8 and 9), using M4 and Problem 2.

	Min. [N]		Max. [N]		Std. [N]	
	Meas.	Pred.	Meas.	Pred.	Meas.	Pred.
250 km/h	99.11	102.97	178.61	169.68	13.75	12.38
275 km/h	91.62	97.74	191.49	181.53	21.49	18.33

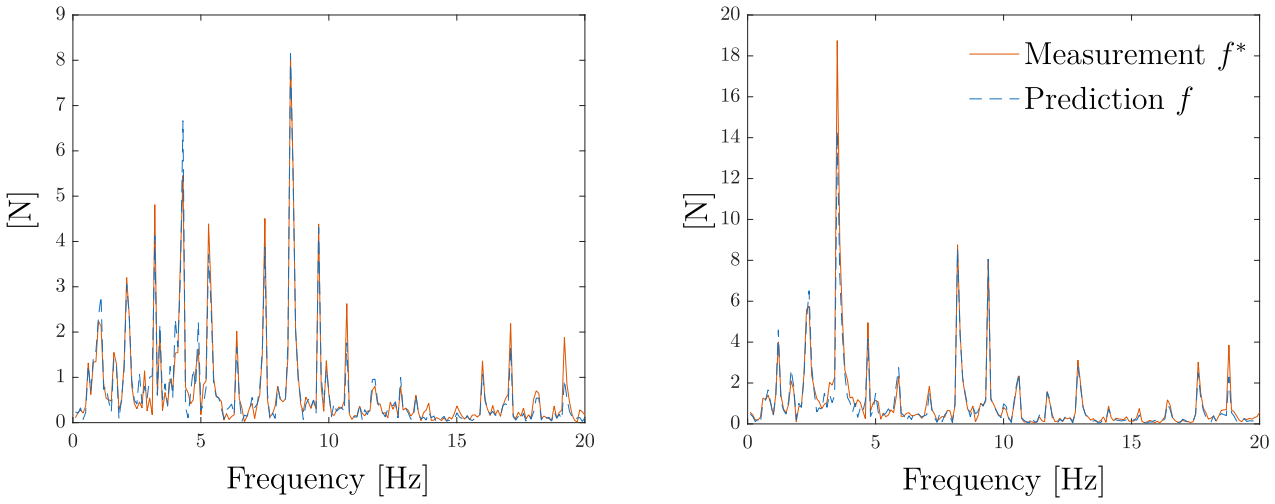


Fig. 14. M4 validation results of Problem 1: Catenary signals at 250 km/h (left) and 275 km/h (right) in the frequency domain.

Table 7
Error metrics of predicted contact force in the higher frequency range (Hi) for tests with catenary signals at 250 and 275 km/h (test 8 and 9) using Model 4 in Problem 2.

		MAE [N]	RMSE [N]	NMSE [%]	ρ [-]
Hi	250 km/h	3.99	5.18	14.08	0.93
	275 km/h	5.15	6.38	8.76	0.96

Table 8
Error metrics of predicted contact force in the higher frequency range (Hi) for tests with catenary signals at 225, 250, 275 and 300 km/h with centred (C) and eccentric (E) contact force, using M4 and Problem 2.

		MAE [N]	RMSE [N]	NMSE [%]	ρ [-]
Hi	225 km/h C	4.03	5.18	19.64	0.90
	225 km/h E	2.94	3.74	17.10	0.91
	250 km/h C	4.52	5.73	13.72	0.93
	250 km/h E	3.34	4.33	13.10	0.93
	275 km/h C	5.68	7.02	7.89	0.97
	275 km/h E	5.52	6.74	8.44	0.97
	300 km/h C	5.56	7.00	8.76	0.97
	300 km/h E	4.43	5.54	10.09	0.96

6.3.1. Eccentric force

The approach proposed in this work uses the acceleration/displacement measured at the center of the contact strips to predict the contact force. As discussed in Section 2, this prediction could be done independently of the contact force position. To verify this assumption, Tests 7, 8, 9, and 10 in Table 2 were repeated (8 tests) with the contact force applied both at the center of the contact strips and at a point with an eccentricity of $e = 215$ mm. The error metrics obtained for the high-frequency component of the contact force are reported in Table 8. The results show no increase in prediction error due to the change in the contact force position even though the training was performed with the contact force applied at the center. The same tests are illustrated in Fig. 15. Although the force amplitude is lower in the eccentric cases, the prediction accuracy of the model remains unchanged.

6.3.2. Changing pressure, height, eccentricity and slopes

Section 2 presented the theoretical foundations of the frequency-separation approach. The validity of these assumptions must be assessed under a wide range of operating conditions.

Test 8 in Table 2 (catenary signal at 250 km/h) was repeated while introducing significant variations in the regulator pressure, as shown in Fig. 16. It can be observed that the moving average of the contact force, corresponding to its very low-frequency content, is accurately predicted. Table 9 reports the error metrics for the high-frequency, low-frequency, and total force components. The results show that the prediction error in the high-frequency range does not increase in the presence of pressure variations. Furthermore, the errors associated with the low-frequency component remain very small. It should be noted that the values marked with † are not

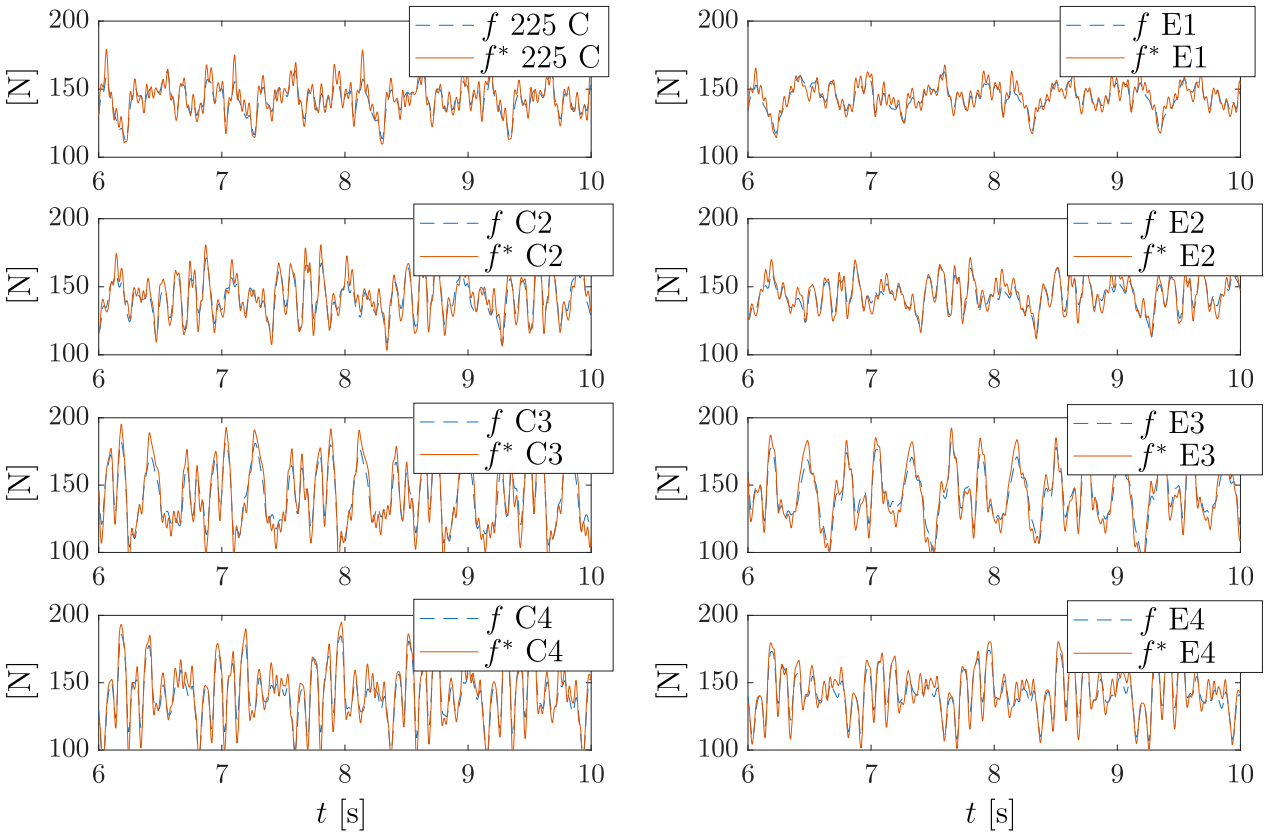


Fig. 15. Tests with Catenary signals at 225, 250, 275 and 300 km/h with centred (C) and eccentric (E) contact force, using M4 and Problem 2.

Table 9
Error metrics of predicted contact force in the higher (Hi), lower (Lo) and total (To) frequency range for tests with catenary signals at 250 km/h without changing pressure of the regulator (no mark) and changing pressure (P), using M4 and Problem 2.

		MAE [N]	RMSE [N]	NMSE [%]	ρ [-]
Hi	250 km/h	3.99	5.18	14.08	0.93
	250 km/h P	4.38	5.59	14.69	0.92
Lo	250 km/h	0.37	0.44	144.09 †	-0.25 †
	250 km/h P	0.31	0.37	0.01	1.00
To	250 km/h	4.02	5.14	13.95	0.93
	250 km/h P	4.36	5.55	2.65	0.99

meaningful because, in the absence of pressure variations, the low-frequency component of the contact force has negligible amplitude. Consequently, relative error metrics and correlation coefficients are not applicable in those cases.

To further validate the proposed method under different operating conditions, Test 9 in Table 2 (catenary signal at 275 km/h) was repeated involving significant regulator pressure variations and four different configurations (C+, E+, C-and E-) combining centered (C) and eccentric (E) contact force and pantograph heights 200 mm below (-) and 200 mm above (+) the reference position. Model M4 and Problem 2 were used for all predictions. Table 10 summarizes the error metrics obtained for these tests. It can be observed that the prediction errors remain very similar across the four configurations for all frequency ranges, with only a slight increase in the low-frequency error when the pantograph is lowered (-). Furthermore, the errors in the high-frequency range are comparable to those obtained in the tests without pressure variations and at the reference height (second row of Table 7). The prediction accuracy in the very low-frequency range is illustrated in Fig. 17(a), which compares the predicted and measured contact forces after low-pass filtering. The results indicate that the relationship between the contact force and the bellows pressure can be considered linear.

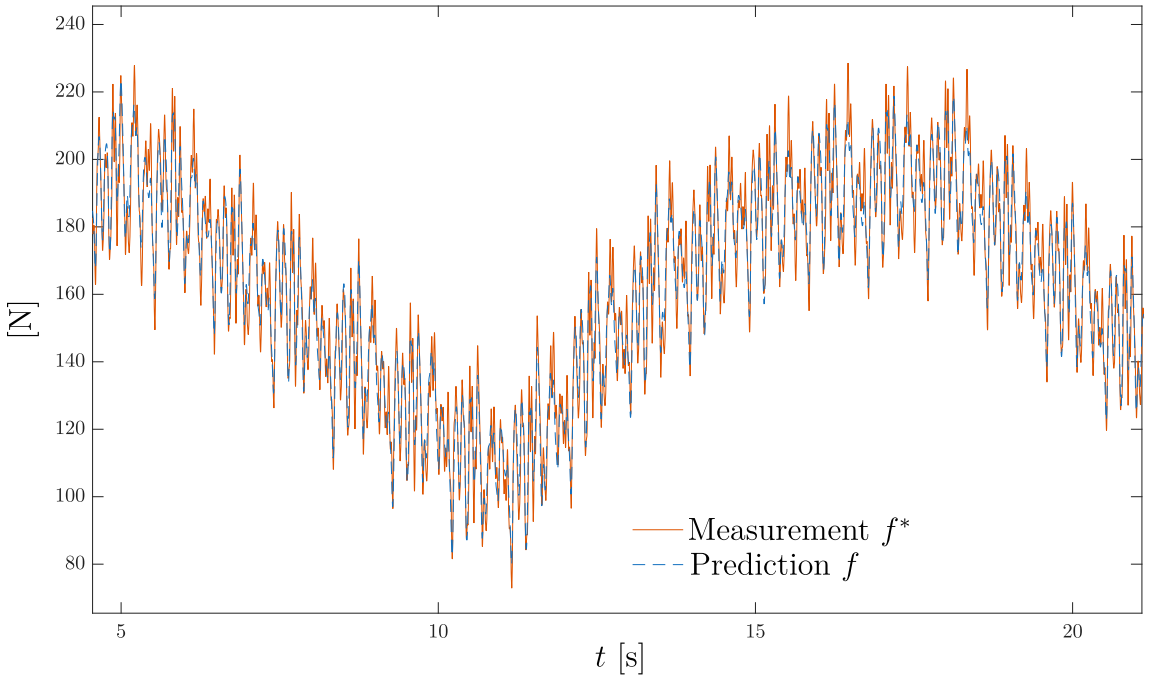


Fig. 16. Test with Catenary signals at 250 km/h with change in pressure induced by regulator, using M4 and Problem 2.

Table 10
Error metrics of predicted contact force in the higher (Hi), lower (Lo) and total (To) frequency range for tests with catenary signals at 275 km/h changing pressure with the regulator. Tests with centered (C) and eccentric (E) contact force, and lower (−) and higher (+) pantograph height, using M4 and Problem 2.

		MAE [N]	RMSE [N]	NMSE [%]	ρ [-]
Hi	275 km/h C +	7.00	8.72	13.01	0.94
	275 km/h E +	4.73	5.90	9.20	0.96
	275 km/h C −	6.04	7.46	9.09	0.97
	275 km/h E −	5.85	7.16	10.31	0.95
Lo	275 km/h C +	0.63	0.72	0.08	1.00
	275 km/h E +	0.88	0.94	0.07	1.00
	275 km/h C −	1.88	1.94	0.06	1.00
	275 km/h E −	1.38	1.42	0.02	1.00
To	275 km/h C +	7.19	8.84	8.12	0.96
	275 km/h E +	4.93	6.07	4.81	0.98
	275 km/h C −	6.35	7.70	5.54	0.98
	275 km/h E −	6.03	7.26	4.81	0.98

The last feature added to the tests is a displacement of the contact point accounting for catenary slopes, which introduces a significant very low-frequency motion of the contact point. A slope is applied such that the contact point moves from $z = 0$ mm to $z = 200$ mm, then to $z = -200$ mm, and finally back to $z = 0$ mm, at an average vertical speed of 24 mm/s.

Tests 8 and 9 of Table 2 (catenary signal at 250 and 275 km/h) are repeated including slope effects and significant pressure regulator variations for two configurations, with centered (C) and eccentric (E) contact force. The corresponding error metrics are reported in Table 11. It can be observed that the errors in the high-frequency range remain similar to those obtained in the tests without pressure variations and without slope (Table 7). However, in the very low-frequency range, a significant increase in error is observed with respect to the cases without slope (Tables 9 and 10).

This degradation in prediction accuracy in the very low-frequency range can also be observed in Fig. 17(b) compared to Fig. 17(a). The increase in error is attributed to the force exerted by the damper, which becomes more significant for large-amplitude low-frequency motions, leading to a breakdown of the quasi-static assumption. Furthermore, this error increase would be more pronounced for steeper slopes with higher vertical velocities than the 24 mm/s considered here. Slope limits are regulated in Standard EN 50119 [34]. No slopes are permitted above 250 km/h, and a slope of 1/1000 is allowed up to 250 km/h, corresponding to 70 mm/s at that

Table 11
Error metrics of predicted contact force in the higher (Hi), lower (Lo) and total (To) frequency range for tests with catenary signals at 250 and 275 km/h with catenary slope of 24 mm/s and changing pressure with the regulator. Tests with centered (C) and eccentric (E) contact force, using M4 and Problem 2.

		MAE [N]	RMSE [N]	NMSE [%]	ρ [-]
Hi	250 km/h C	4.38	5.52	13.63	0.93
	250 km/h E	3.39	4.35	12.74	0.94
	275 km/h C	6.76	8.30	10.55	0.96
	275 km/h E	5.63	6.93	10.03	0.96
Lo	250 km/h C	2.73	3.10	1.11	1.00
	250 km/h E	2.43	2.71	1.46	0.99
	275 km/h C	2.17	2.52	0.84	1.00
	275 km/h E	1.94	2.21	0.78	1.00
To	250 km/h C	4.97	6.28	5.81	0.97
	250 km/h E	4.09	5.16	5.18	0.97
	275 km/h C	7.03	8.63	7.54	0.97
	275 km/h E	5.81	7.20	5.90	0.97

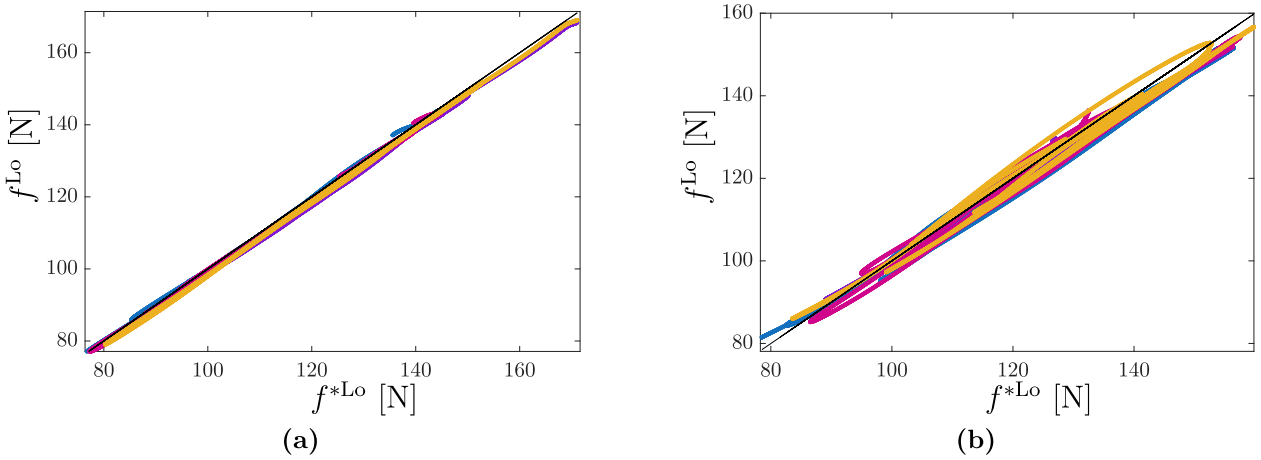


Fig. 17. Predicted vs measured contact force in the low frequency range. (a) Tests of Table 10 and (b) tests of Table 11.

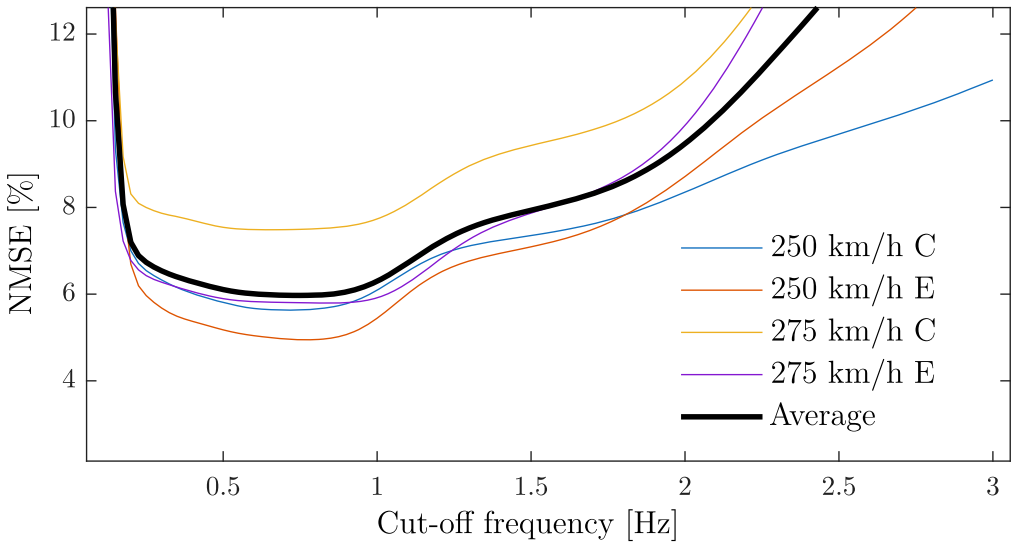


Fig. 18. NMSE with M4 and Problem 2 for tests with presurre changes and slopes (tests of Table 11) with respect to the cut-off frequency. Tests with centered (C) and eccentric (E) contact force.

speed, while higher vertical velocities are permitted at lower speeds. Therefore, the proposed method is applicable in the absence of slopes or under moderate slope conditions, below approximately 24 mm/s, within the error bounds discussed above.

6.3.3. Performance as a function of the cut-off frequency

The cut-off frequency is a key parameter that separates the frequency range in which the force is reconstructed using pressure from the frequency range in which it is reconstructed using displacement and acceleration. The most difficult scenario for this method is found in the tests with slopes and regulator pressure changes. Those tests were included in Table 11, and Fig. 18 shows the NMSE as a function of the cut-off frequency when using M4 and Problem 2. It can be seen that the optimum range is between 0.5 and 1 Hz, and in this work, 0.5 Hz has been adopted.

7. Conclusions

This work addressed the problem of estimating the contact force acting on a railway pantograph by means of a low-intrusive approach, avoiding any structural modification of the system. The proposed methodology combines pressure measurements from the uplift mechanism with displacement and acceleration measurements on the contact strips center, enabling the reconstruction of the contact force over the frequency range of interest defined by EN 50317 [2].

A two-stage estimation strategy was introduced, in which the very low-frequency component of the contact force is obtained from the pressure signal through a calibrated linear relationship, while the higher-frequency content is reconstructed from acceleration and displacement measurements using inverse dynamic models.

Four estimation models were implemented and compared, including two model-based approaches and two data-driven artificial intelligence models. The comparison was carried out under identical experimental conditions and with parameter optimisation for each method, ensuring a fair assessment of their best achievable performance. Furthermore, two measurement configurations were analysed: acceleration combined with displacement and acceleration only, allowing the influence of displacement measurements on estimation accuracy to be quantified.

The implementation was performed on a laboratory test bench with a real pantograph DSA-380 and a directly measured contact force for assessing the method. The results demonstrate that the proposed low-intrusive framework is capable of reconstructing the contact force with reasonably accuracy within the target frequency range. The study also highlights the differences between model-based and data-driven approaches, as well as the non-necessity of including displacement measurements. Neural Networks and Long Short-Term Memory networks achieved the best performance in predicting the external force, although the Kalman filter exhibited only a modest increase in error.

The proposed method provides reasonable estimation errors in both low and high frequency ranges under variations of contact force eccentricity, pantograph height, and regulator-induced pressure changes. The results show that the approach is robust to these operating conditions, maintaining consistent performance across all tested scenarios.

In particular, a key result is that the contact force can be accurately predicted even when it is applied with significant eccentricity, despite the fact that the method only uses acceleration/displacement measurements at the center of the contact strips and the training/optimisation was performed with the contact force applied at the center.

The method also performs adequately under moderate catenary slope conditions. However, for higher vertical velocities (higher than 24 mm/s), the error in the low-frequency prediction increases, indicating that the quasi-static assumption becomes less accurate and the method should be applied with caution in such cases for predicting the very-low frequency range of the contact force.

It is important to note that all results are valid for the DSA 380 pantograph and the specific range of conditions considered in this study. Since this work is carried out on a laboratory test rig, aerodynamic effects and inertial forces associated with train motion are outside the scope of the proposed reconstruction method. Their influence must be assessed under real operating conditions. Further work is required to assess the applicability and robustness of the proposed approach under different pantograph designs and operating environments.

Overall, the work advances the state of the art in pantograph contact force monitoring by providing an experimentally validated, low-intrusive estimation framework and a systematic comparison of different modelling paradigms. The proposed methodology represents a practical step towards simplified and less invasive contact force monitoring potentially in on-track applications.

CRediT authorship contribution statement

J. Gil: Writing – original draft, Software, Methodology, Investigation, Conceptualization; **M. Tur:** Supervision, Resources, Investigation, Funding acquisition; **S. Gregori:** Writing – review & editing, Visualization, Investigation, Conceptualization; **F. J. Fuenmayor:** Validation, Supervision, Project administration.

Declaration of competing interest

The authors declare that they have no known competing financial interests or personal relationships that could have appeared to influence the work reported in this paper.

Acknowledgment

The authors would like to express their gratitude for the financial support received from the State Research Agency of the Spanish Science and Innovation Ministry (PID2023-148854OB-C21).

Data availability

Data will be made available on request.

References

[1] S. Bruni, J. Ambrosio, A. Carnicero, Y.H. Cho, L. Finner, M. Ikeda, S.Y. Kwon, J.P. Massat, S. Stichel, M. Tur, The results of the pantograph-catenary interaction benchmark, Veh. Syst. Dyn. 53 (3) (2015) 412–435.
[2] EN 50317, Railway applications. current collection systems. requirements for and validation of measurements of the dynamic interaction between pantograph and overhead contact line, Eur. Comm. Electrotech. Stand. (2012).
[3] D. Simon, Optimal State Estimation: Kalman, H Infinity, and Nonlinear Approaches, Wiley-Interscience, 2006.
[4] E. Lourens, E. Reynders, G. De Roeck, G. Degrande, G. Lombaert, An augmented Kalman filter for force identification in structural dynamics, Mech. Syst. Signal Process. 27 (2012) 446–460. https://doi.org/10.1016/j.ymssp.2011.09.025
[5] P.K. Kitanidis, Unbiased minimum-variance linear state estimation, Automatica 23 (6) (1987) 775–778. https://doi.org/10.1016/0005-1098(87)90037-9
[6] M. Darouach, M. Zasadzinski, M. Boutayeb, Extension of minimum variance estimation for systems with unknown inputs, Automatica 39 (5) (2003) 867–876. https://doi.org/10.1016/S0005-1098(03)00006-2
[7] S. Pan, P. Du, Y. Li, Z. Chen, H. Wang, The study on an general Kalman filter with unknown inputs, in: Proceeding of the 11th World Congress on Intelligent Control and Automation, 2014, pp. 3562–3567. https://doi.org/10.1109/WCICA.2014.7053308
[8] S. Gillijns, B. De Moor, Unbiased minimum-variance input and state estimation for linear discrete-time systems, Automatica 43 (1) (2007) 111–116. https://doi.org/10.1016/j.automatica.2006.08.002
[9] C.-S. Hsieh, Robust two-stage Kalman filters for systems with unknown inputs, IEEE Trans. Autom. Contr. 45 (12) (2000) 2374–2378. https://doi.org/10.1109/9.895577
[10] C.-K. Ma, C.-C. Ho, An inverse method for the estimation of input forces acting on non-linear structural systems, J. Sound Vib. 275 (3) (2004) 953–971. https://doi.org/10.1016/S0022-460X(03)00797-1
[11] N. Yilmaz, J.Y. Wu, P. Kazanzides, U. Tumerdem, Neural network based inverse dynamics identification and external force estimation on the da vinci research kit, in: 2020 IEEE International Conference on Robotics and Automation (ICRA), 2020, pp. 1387–1393. https://doi.org/10.1109/ICRA40945.2020.9197445
[12] S.A. Shaikh, H. Cherukuri, T. Khan, Recovering the forcing function in systems with one degree of freedom using ANN and physics information, Algorithms 16 (5) (2023). https://doi.org/10.3390/a16050250
[13] Y. Yu, X. Si, C. Hu, J. Zhang, A review of recurrent neural networks: LSTM cells and network architectures, Neural Comput. 31 (2019) 1235–1270. https://doi.org/10.1162/neco_a_01199
[14] T.-C. Callar, S. Bottger, Hybrid learning of time-series inverse dynamics models for locally isotropic robot motion, IEEE Robot. Autom. Lett. 8 (2) (2023) 1061–1068. https://doi.org/10.1109/lra.2022.3222951
[15] W. Huang, Y. Lin, M. Liu, H. Min, Velocity-aware spatial-temporal attention LSTM model for inverse dynamic model learning of manipulators, Front. Neurorobotics 18 (2024) 1353879. https://doi.org/10.3389/fnbot.2024.1353879
[16] C. Huang, C. Tao, H. Ji, J. Qiu, Impact force reconstruction and localization using distance-assisted graph neural network, Mech. Syst. Signal Process. 200 (2023) 110606. https://doi.org/10.1016/j.ymssp.2023.110606
[17] M. Bocciolone, G. Bucca, A. Collina, L. Comolli, Comparison of optical and electrical measurements of the pantograph-catenary contact force, in: J.L. Santos, B. Culshaw, J.M. López-Higuera, W.N. MacPherson (Eds.), Fourth European Workshop on Optical Fibre Sensors, 7653, International Society for Optics and Photonics, SPIE, 2010, p. 765346. https://doi.org/10.1117/12.866357
[18] S. Gao, Automatic detection and monitoring system of pantograph-catenary in China's high-speed railways, IEEE Trans. Instrum. Meas. 70 (2021) 1–12. https://doi.org/10.1109/TIM.2020.3022487
[19] S. Liu, Y. Wei, Y. Yin, T. Feng, J. Lin, Structural health monitoring method of pantograph-catenary system based on strain response inversion, Front. Phys. Volume 9 - 2021 (2021). https://doi.org/10.3389/fphy.2021.691510
[20] M. Carnevale, A. Collina, Processing of collector acceleration data for condition-based monitoring of overhead lines, Proc. Inst. Mech. Eng. F: J. Rail Rapid Transit 230 (2) (2016) 472–485. https://doi.org/10.1177/0954409714545637
[21] H. Wang, Z. Liu, A. Núñez, R. Dollevoet, Identification of the catenary structure wavelength using pantograph head acceleration measurements, in: 2017 IEEE International Instrumentation and Measurement Technology Conference (I2MTC), 2017, pp. 1–6. https://doi.org/10.1109/I2MTC.2017.7969731
[22] A. Collina, F. Fossati, M. Papi, F. Resta, Impact of overhead line irregularity on current collection and diagnostics based on the measurement of pantograph dynamics, Proc. Inst. Mech. Eng. F J. Rail Rapid Transit 221 (4) (2007) 547–559. https://doi.org/10.1243/09544097F02105
[23] H. Chen, N. Zhou, W. Zhang, Non-contact contact force estimation for pantograph and catenary system based on Kalman filter, in: W. Huang, M. Ahmadian (Eds.), Advances in Dynamics of Vehicles on Roads and Tracks III, Springer Nature Switzerland, Cham, 2025, pp. 41–50.
[24] C.-C. Ho, C.-K. Ma, Active vibration control of structural systems by a combination of the linear quadratic Gaussian and input estimation approaches, J. Sound Vib. 301 (3) (2007) 429–449. https://doi.org/10.1016/j.jsv.2005.12.061
[25] R. Zhou, X. Xu, Contact force surrogate model and its application in pantograph-catenary parameter optimization, Appl. Sci. 14 (1) (2024). https://doi.org/10.3390/app14010448
[26] Y. Song, H. Wang, G. Frøseth, P. Nåvik, Z. Liu, A. Rønnquist, Surrogate modelling of railway pantograph-catenary interaction using deep long-short-term-memory neural networks, Mech. Mach. Theory 187 (2023) 105386. https://doi.org/10.1016/j.mechmachtheory.2023.105386
[27] G. Huang, G. Wu, Z. Yang, X. Chen, W. Wei, Development of surrogate models for evaluating energy transfer quality of high-speed railway pantograph-catenary system using physics-based model and machine learning, Appl. Energy 333 (2023) 120608. https://doi.org/10.1016/j.apenergy.2022.120608
[28] W. Chu, H. Wang, Y. Song, Z. Liu, FENet: a physics-informed dynamics prediction model of pantograph-catenary systems in electric railway, IET Intell. Transp. Syst. 19 (1) (2025) e70059. https://doi.org/10.1049/itr2.70059
[29] M. Wu, X. Xu, H. Zhang, R. Zhou, J. Wang, Pantograph-catenary interaction prediction model based on SCSA-RBF network, Appl. Sci. 14 (1) (2024). https://doi.org/10.3390/app14010449
[30] S. Gregori, M. Tur, J. Gil, F.J. Fuenmayor, Assessment of catenary condition monitoring by means of pantograph head acceleration and artificial neural networks, Mech. Syst. Signal Process. 202 (2023). https://doi.org/10.1016/j.ymssp.2023.110697
[31] L. Ale, Y. Song, Z. Liu, H. Xing, H. Liang, Real-time prediction of high-speed rail pantograph-catenary contact force using deep learning framework, Veh. Syst. Dyn. (2026) 1–23. https://doi.org/10.1080/00423114.2025.2606345
[32] D.A. Allan, J.B. Rawlings, Moving Horizon Estimation, Springer International Publishing, Cham, 2019, pp. 99–124. https://doi.org/10.1007/978-3-319-77489-3_5
[33] L. Zou, Z. Wang, J. Hu, D. Zhou, Moving horizon estimation with unknown inputs under dynamic quantization effects, IEEE Trans. Autom. Contr. 65 (12) (2020) 5368–5375. https://doi.org/10.1109/TAC.2020.2968975
[34] EN 50119:2021, Railway applications. fixed installations. electric traction overhead contact lines, Eur. Comm. Electrotech. Stand. (2021).